Available online at www.sciencedirect.com
SCIENCE DIRECT®
International Journal of Heat and Mass Transfer 48 (2005) 4704–4725
International Journal of HEAT and MASS TRANSFER
www.elsevier.com/locate/ijhmt

Unsteady RANS simulation of turbulent flow and heat transfer in ribbed coolant passages of different aspect ratios

Arun K. Saha, Sumanta Acharya *

Department of Mechanical Engineering, Louisiana State University, Baton Rouge, LA 70803, United States

Received 9 July 2004; received in revised form 27 May 2005
Available online 1 September 2005

Abstract

The flow and heat transfer in ribbed coolant passages of aspect ratios (AR) 1:1, 4:1, and 1:4 are numerically studied through the solution of the unsteady Reynolds averaged Navier–Stokes (URANS) equations. The URANS procedure, which utilizes a two equation k–ε model for the turbulent stresses, is shown to resolve large-scale bulk unsteadiness. The computations are carried out for a fixed Reynolds number of 25,000 and density ratio of 0.13, while the Rotation number is varied between 0.12 and 0.50.

At higher rotation numbers ($\geqslant 0.5$) at least three inter-rib modules are required to ensure periodicity in the streamwise direction. The flow exhibits unsteadiness in the Coriolis-driven secondary flow and in the separated shear layer. The average duct heat transfer is the highest for the 4:1 AR case. For this case, the secondary flow structures consist of multiple roll cells that direct flow both to the trailing and leading surfaces. The 1:4 AR duct shows flow reversal along the leading surface at high rotation numbers. For this AR, the potential for conduction-limited heat transfer along the leading surface is identified. The friction factor reveals an increase with the rotation number, and shows a significant increase at higher rotation numbers ($\sim Ro = 0.5$).

1. Introduction

In internal cooling of gas turbine blades, coolant air is circulated through serpentine passages and discharged through the bleed holes along the trailing edge of the blade (Fig. 1(a)). With rotation, the flow is subjected to Coriolis forces and centrifugal-buoyancy effects. The Coriolis forces induces secondary flow in planes perpendicular to the streamwise flow direction; this causes the migration of core fluid towards the trailing wall for radially-outward flow. Thus, rotation destabilizes the flow and enhances heat transfer along the trailing wall while they stabilize the flow and reduces the heat transfer along the opposite wall. In addition, centrifugal buoyancy influences the radially-outward flow along the heated walls and, at high rotation numbers, can have a significant effect on the surface heat transfer.

The cross-section of a turbine blade varies considerably over its axial chord as its thickness changes from the front leading edge to the trailing edges. The aspect ratio (AR) of the coolant passage, defined as the ratio of the width of the leading or trailing walls (B) to the height of the sidewalls (H), varies from low values (e.g., 1:4–1:6) near the thickest-portion of the blade to high values (e.g., 4:1–10:1) near the trailing edge. Near the mid-chord regions, the coolant passage is almost

* Corresponding author. Tel.: +1 225 578 5809; fax: +1 225 578 5924.
E-mail address: acharya@me.lsu.edu (S. Acharya).

0017-9310/$ - see front matter © 2005 Published by Elsevier Ltd.
doi:10.1016/j.ijheatmasstransfer.2005.05.030

Nomenclature

B	width of the duct
Bo	buoyancy parameter, $(\Delta\rho/\rho)Ro^2R_M$
D_h	hydraulic diameter of the duct, $4HB/(2(H+B))$
e	size of the square ribs
f	friction factor, $[\Delta p_x/(0.5\rho u_{av}^2)]$
h	local heat transfer coefficient
H	height of the duct
K_f	ratio of thermal conductivity of fluid to that of solid
L_x	streamwise extent of the periodic domain
Nu	Nusselt number, $hB/K_f = -((\partial\theta/\partial n)\|_{n=0})/(\theta_w(x,y)-\theta_b(x))$
P	pitch of the ribs
p	periodic component of pressure
Pr	Prandtl number, ν/α
q_j	turbulent thermal subgrid stress
Re	Reynolds number, $u_{av}B/\nu$
r_j	radius of rotation
R_M	mean radius of rotation
Ro	rotation number, $\Omega B/u_{av}$
t	time
T	temperature
u, v, w	non-dimensional velocity in x-, y-, and z-directions
u', v', w'	non-dimensional velocity fluctuations in x-, y-, and z-directions
u_τ	frictional velocity, $\sqrt{(\tau_w/\rho)}$
Y^+	yu_τ/ν
x, y, z	non-dimensional Cartesian coordinates

Greek symbols

α	thermal diffusivity
$\beta(t)$	mean pressure gradient
ε_{ijk}	alternating tensor
δ_{ij}	Kronecker delta
θ	non-dimensional periodic component of temperature, $(T-T_w)/(T_{m1}-T_w)$
ρ	density of the fluid
$\Delta\rho/\rho$	coolant-to-density ratio, $(T_w-T_b)/T_w$
ω_i	instantaneous vorticity, $\varepsilon_{ijk}\partial u_k/\partial x_j$
ν	kinematic viscosity of the fluid
τ_{ij}, τ_w	turbulent stress and wall shear stress, $\mu\partial u/\partial n\|_{n=0}$, respectively

square in cross-section (AR of 1:1), and this AR duct has been extensively studied in the literature. However, the low and high AR ducts have received considerably less attention in the literature, and since the strength and the pattern of the secondary flow are expected to be influenced by the AR, there is a need to investigate the effect of the AR particularly for parameter ranges of relevance to engine conditions.

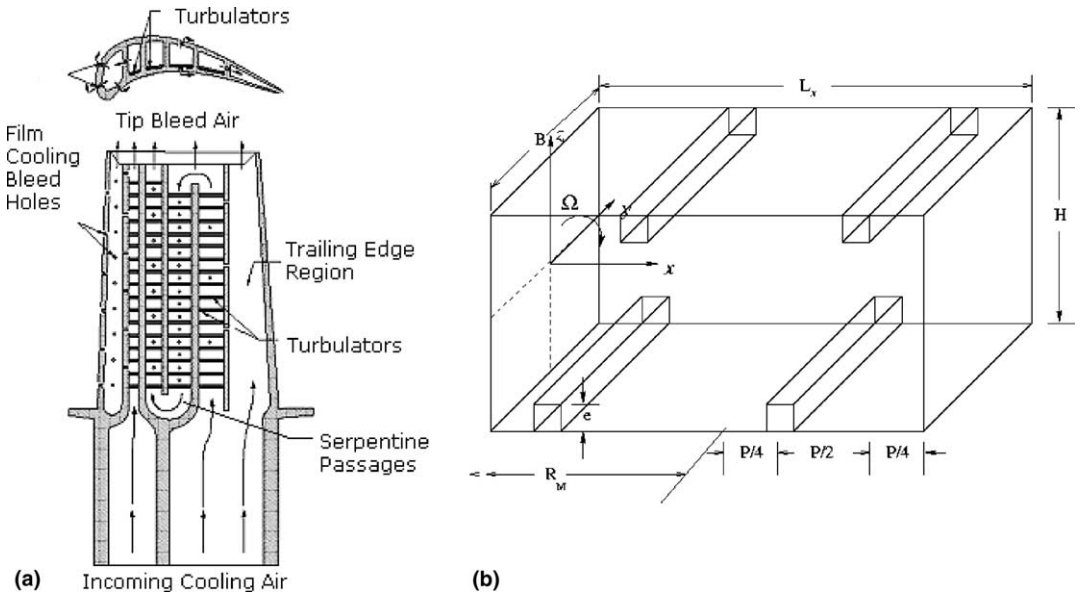

Fig. 1. (a) Schematic of internal cooling strategy (taken from Wagner et al. [3]) and (b) three-dimensional computational model for turbine blade.

A large number of experimental studies are reported in the literature on internal cooling in turbine blade passages, particularly for square (AR = 1:1) coolant passages [1–6]. In a recent study, heat transfer in a rectangular channel with aspect ratio AR = 4:1 has been reported by Zhou et al. [7] for smooth surfaces and by Griffith et al. [8] for rib-roughened surfaces. Non-monotonic behavior with respect to the rotation number was observed for the smooth channel [7], while for the ribbed channel, the trailing surface heat transfer shows strong dependence on the rotation number [8]. Data for 1:4 AR duct with rotation is similarly limited, with Agarwal et al. [9] recently reporting mass transfer data for smooth and ribbed ducts with rotation.

Most of the earlier computational studies on internal cooling passage of the blades have been restricted to three-dimensional steady RANS (SRANS) simulations [10–12]. The flow and heat transfer through a two-pass smooth and 45° rib-roughened rectangular duct with an aspect ratio of 2 has been reported by Al-Qahtani et al. [13,14] using a Reynolds stress turbulence model. They have found reasonable match with experiments, although in certain regions there are significant discrepancies. In these studies (e.g., [14]), the maximum rotation numbers considered have been limited to 0.28.

A key deficiency of steady Reynolds averaged Navier–Stokes simulation (SRANS) procedure is their inability to properly represent the unsteady dynamics of large-scale structures in the turbulence model. Direct numerical simulation (DNS), large eddy simulation (LES) and unsteady RANS (URANS) provide alternative approaches where all or a portion of the unsteady spectrum is resolved. In DNS all scales are resolved, and no modeling is introduced. In LES, all dynamics of turbulent eddies above a cut-off filter (twice the mesh size) are resolved while only the smaller-scale fluctuations are modeled. In URANS, all turbulent fluctuations are modeled while only the unsteadiness in the large-scale bulk motions is resolved. Thus, URANS aims to capture only the first few fundamental frequencies and models the remaining spectrum of fluctuating motions using a standard turbulence closure.

Flow through a rotating square smooth duct has been simulated using LES by Pallares and Davidson [15]. Saha and Acharya [16] reported good comparison of URANS with the LES results reported in [15]. They also reported similar comparisons for a rotating 1:1 AR ribbed duct, and concluded that the time-averaged URANS and LES predictions agree well with measurements, and with each other. Murata and Mochizuki [17,18] carried out an LES study of flow and heat transfer in an orthogonally rotating rectangular duct having AR of 1:1, 1:2 and 1:4 with in-line transverse and 60°-angled ribs. It was observed that the smaller aspect ratio cases are most affected by the rotation and this effect increases with rotation number.

There are only a limited number of studies that explore the role of aspect ratio on the fluid flow and heat transfer in a rotating ribbed duct. Very few of these studies incorporate or accurately represent the effect of flow unsteadiness, and further, none of these studies have examined aspect ratio effects at high rotation numbers where flow unsteadiness plays an important role. The goal of the present paper is to use URANS to study the effect of aspect ratio and rotation number for parameter ranges of relevance to gas turbine industry. In the present study, three ARs of 1:1, 4:1, and 1:4 are studied for a Reynolds number (Re) and density ratio (DR) of 25,000 and 0.13, respectively, and for rotation numbers (Ro) in the range of 0.12–0.50. It should be noted that unsteady flow calculations such as URANS and LES for the above-noted parameter ranges (specifically high Ro) have not been previously reported for the 4:1 and 1:4 AR geometries. In addition, there is no experimental data in this parameter regime for all three ARs that will enable a comparative assessment of AR effects.

2. Mathematical model

The geometrical model of the problem to be studied is presented in Fig. 1(b). The ribs of dimensions, $e \times e$, form a periodic pattern with streamwise pitch of L_x. The periodic module in the streamwise direction consists of two or three ribs depending on AR and Ro. Preliminary studies indicated that a periodic module consisting of one rib suppressed unsteadiness at low Reynolds number and rotation, while periodic modules containing two or more ribs were able to sustain large-scale unsteadiness. The working fluid chosen in the present study is air whose Prandtl number is 0.7.

2.1. Governing equations

The unsteady Navier–Stokes equations, the continuity equation and the energy equation have been numerically solved in the present study. In dimensionless form these equations are expressed as

$$\frac{\partial \langle u \rangle_i}{\partial x_i} = 0 \tag{1}$$

$$\frac{\partial \langle u \rangle_i}{\partial t} + \frac{\partial}{\partial x_j}\left(\langle u \rangle_j \langle u \rangle_i\right) = -\frac{\partial \langle p \rangle}{\partial x_i} + \delta_{i1}\beta(t) + \frac{1}{Re}\frac{\partial^2 \langle u \rangle_i}{\partial x_j^2} + \frac{\partial \tau_{ij}}{\partial x_j} - 2Ro\varepsilon_{i2k}\langle u \rangle_k - \frac{Bo}{R_M}(1-\theta)\varepsilon_{i2l}\varepsilon_{l2k} r_k \tag{2}$$

$$\frac{\partial \langle \theta \rangle}{\partial t} + \langle \theta \rangle \Lambda + \frac{\partial}{\partial x_j}\left(\langle u \rangle_j \langle \theta \rangle\right) = \frac{1}{RePr}\frac{\partial^2 \langle \theta \rangle}{\partial x_j^2} + \frac{\partial q_j}{\partial x_j} \tag{3}$$

where $\beta(t)$ is the linear component of the non-dimensional pressure that has to be adjusted at each time step to get the desired mass flow rate, $\langle\theta\rangle = (\langle T\rangle - \langle T\rangle_w)/(\langle T\rangle_{m1} - \langle T\rangle_w)$, $\tau_{ij} = -\overline{u_i' u_j'}$ and $q_j = -\overline{u_j'\theta'}$. The terms τ_{ij} and q_j in Eqs. (2) and (3) are the turbulent stress and flux contributions that have to be modeled. Here, $\langle T\rangle_w$ is the wall temperature and $\langle T\rangle_{m1}$ is the bulk temperature of the fluid evaluated at the inlet section of the computational domain. The unknown function Λ in the energy equation is given by

$$\Lambda = \frac{1}{\langle T\rangle_{m1} - \langle T\rangle_w}\frac{\partial}{\partial t}(\langle T\rangle_{m1} - \langle T\rangle_w)$$

The coupling between $\bar{\theta}$ and Λ can be solved iteratively as described by Wang and Vanka [19]. In the above equations the velocities are non-dimensionalized with the average velocity $\langle u_{av}\rangle$, all lengths are scaled with the hydraulic diameter of the duct, D_h, pressure is scaled with $\rho\langle u_{av}\rangle^2$ and time is scaled by $D_h/\langle u_{av}\rangle$.

2.2. Unsteady RANS turbulence model

The URANS calculations have been carried out using a two-equation ($\langle k\rangle$ and $\langle\varepsilon\rangle$) model of Kato and Launder [20]. The Kato and Launder [20] model is found to be suitable for bluff body flows since it can handle the stagnation zone properly by reducing the turbulent production in this region. In this model [20], the turbulence closure for τ_{ij} and q_j is based on the gradient transport hypothesis, but the production of turbulent kinetic energy is written in terms of rotation and shear of fluid elements instead of only shear.

2.3. Boundary conditions

The periodic boundary conditions for velocities, pressure and turbulence quantities in the streamwise direction can be written as

$$\langle\phi\rangle(x + nL_x, y, z, t) = \langle\phi\rangle(x, y, z, t) \tag{4}$$

where $\phi \equiv (u_i, p, k, \varepsilon)$, L_x is the streamwise length of each inter-rib module, and n represents the number of inter-rib modules included in the computational domain. The corresponding periodic boundary conditions for the energy equations are

$$\frac{\langle\theta\rangle(x + nL_x, y, z, t)}{\langle\theta\rangle_{m2}} = \frac{\langle\theta\rangle(x, y, z, t)}{\langle\theta\rangle_{m1}} \tag{5}$$

where $\langle\theta\rangle_{m1}$ and $\langle\theta\rangle_{m2}$ are the non-dimensional bulk temperatures at the inlet and outlet of the computational domain, respectively.

The channel and obstacle surfaces are treated as no-slip boundaries. All the walls are heated ($\langle\theta\rangle_w = 0$). The normalized kinetic energy is set to zero at all solid surfaces while zero Neumann boundary conditions are used for the non-dimensional dissipation. For near wall modeling, standard wall functions are used and grids are generated such that the Y^+ values of the near-wall grid points lie between 15 and 40.

3. Solution method

The differential equations (1)–(3) are solved on a staggered grid by using a modified version of the MAC algorithm of Harlow and Welch [21]. In each time step, the term, τ_{ij} is calculated by solving the transport equations for k and ε. In the present study, the convective and diffusion terms are approximated by a third-order upwinding scheme of Kawamura et al. [22] and a second-order central differencing scheme, respectively. An explicit, second-order, Adams–Bashforth differencing scheme is used for the time advancement of the convection and diffusion terms. Once the corrected velocities are obtained using continuity and momentum equations, the energy equation is solved using second-order temporal (Adams–Bashforth) integration scheme. The details of the numerical method are described elsewhere [23].

A non-uniform mesh with cells packed towards all the solid boundaries has been used to resolve the near-wall viscous effects. The results were tested for grid independence by comparing the results obtained for a single-rib periodic module square duct with $50 \times 32 \times 42$ and $62 \times 48 \times 50$ grid cells. With the two grids, the surface-averaged Nusselt number along the side walls show a difference of 2.7% while the leading and trailing walls reveal a discrepancy of 1.6% and 1.7%, respectively. The grids for both one inter-rib and two inter-rib periodic module(s) are the same in the vertical and transverse directions, while in the streamwise direction the number of cells is doubled for the two inter-rib periodic module. Therefore, all the computations for the two inter-rib periodic modules are carried out using a grid size of $122 \times 48 \times 50$, and are expected to be grid independent. For the 1:4 AR duct, the grid points in the vertical-height direction are increased and a mesh size of $122 \times 48 \times 78$ is used, while for the 4:1 AR duct the grid points in the transverse-width directions are increased and computations are carried out using a mesh size of $122 \times 72 \times 58$.

Since the present method is an explicit one, the time-step is selected using CFL criterion. For time-averaged fields, the averaging is done for at least 15 flow-through times which results in a total number of time-steps in the range of 6×10^4–10^5.

The present code has been validated thoroughly for the flow and heat transfer characteristics in a channel flow with a periodic array of cylinders [24]. The code has also been validated against published results for the flow past a square cylinder placed in an infinite medium. The computed drag coefficient and the Strouhal

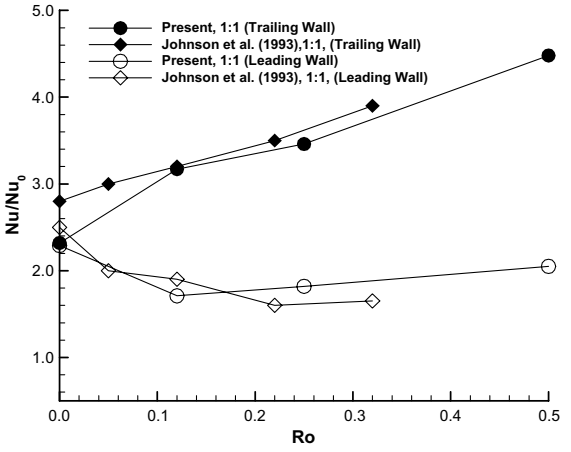

Fig. 2. Comparison of Nusselt number ratio with data.

number match well with the experimental results, and are reported in Saha et al. [25].

For the purposes of the present paper, the present code has been further validated by comparing the present URANS predictions with published velocity measurements for a rotating ribbed duct (AR 1:1) reported by Iacovides [12] for a $Re = 100{,}000$, and heat transfer data reported by Johnson et al. [5] at $Re = 12{,}500$. The match between the streamwise velocity measurements in [12] and the present predictions are quite good, and are presented in detail elsewhere [16]. The Nusselt number comparison with the data in [5], in the periodically-developed region, is shown in Fig. 2, and the present predictions are seen to agree well with the measurements along both the ribbed leading and trailing surfaces.

4. Results and discussions

The computational domain of interest (Fig. 1(b)), represents a periodic module in the radially outward flowing leg of a coolant passage. As noted earlier, two inter-rib modules were needed to sustain flow unsteadiness in the URANS calculations at low *Re* and *Ro*. However, at high rotation numbers (order of 0.5), even the two inter-rib periodic module calculations do not exhibit periodicity for the 1:1 and 4:1 AR ducts. The effect of domain size at high rotation number is discussed below.

In all cases, the ribs are oriented normal to the flow and placed in a staggered fashion on the leading and trailing surfaces of the duct passage. The pitch-to-rib height ratio is 10 while the rib height-to-hydraulic diameter ratio is 0.1. The mean radius of rotation, R_M, is 49. These geometrical dimensions correspond to the experimental study of Johnson et al. [5]. Results are presented for 1:1, 1:4 and 4:1 AR ducts and *Ro* in the range of 0–0.50. The Reynolds number is held fixed at 25,000 and the density ratio is set to 0.13.

4.1. Effect of domain size (number of inter-rib modules)

To determine the domain size in the streamwise direction that will provide periodic solutions, calculations were carried out for three domain sizes containing one (1P), two (2P) and three (3P) inter-rib(s) modules. At lower rotation numbers, all three AR ducts show periodicity across each inter-rib module. At a *Ro* of 0.5, the 1:1 and 4:1 AR ducts show loss of periodicity across a single inter-rib module. Therefore, the 1:1 AR duct is discussed below to illustrate the effects of the choice of the computational domain size on the flow field and heat transfer. For comparison purposes, only the time-averaged flow and heat transfer field is shown.

Fig. 3(a), (c) and (e) show the vector plots on the mid-transverse plane superimposed on the temperature contours, while the secondary flow structures along with the temperature contours at an axial location $x = 0.5$ are shown in Fig. 3(b), (d) and (f). The overall flow pattern in 1P (Fig. 3(a)) and 3P (Fig. 3(e)) modules look similar. The flow structures in 3P module are seen to be periodic over each inter-rib module. The corresponding temperature field do not show periodicity because of the scaling used where the non-dimensional temperature contains the bulk temperature at the inlet in the denominator. However, when scaled with the local bulk temperature, the temperature field reveals perfect periodicity over each inter-rib periodic domain. The periodicity over each inter-rib domain is lost in the 2P module and can be verified by the different flow field patterns in the two inter-rib domains (Fig. 3(c)). The non-periodic behavior is more evident near the trailing wall while it is not significantly different near the leading wall (see Fig. 4). The loss of periodicity in the 2P module is linked to the development of unsteadiness with wavelengths that are of order 1P. A 2P domain length is not long enough to contain several wavelengths of these large scale disturbances, and a 3P domain size is needed so that the large scale unsteadiness close to the inlet are not strongly correlated with the fluctuations at the exit, enabling periodic conditions to be correctly imposed. For the 1P domain, these large scale fluctuations are completely suppressed, and therefore periodicity appears to be preserved. However, the 1P solution does not include the effect of the large scale fluctuations (order of 1P), and differences between the 1P and the 3P solutions, albeit small, are a consequence of this effect. In examining the secondary flow structures along with the temperature contours at an axial location $x = 0.5$ (Fig. 3(b), (d) and (f)), it can be seen that the overall flow pattern in the 1P and 3P modules generally agree, although there are differences in the sizes of the secondary flow structures and relative strengths and locations. However,

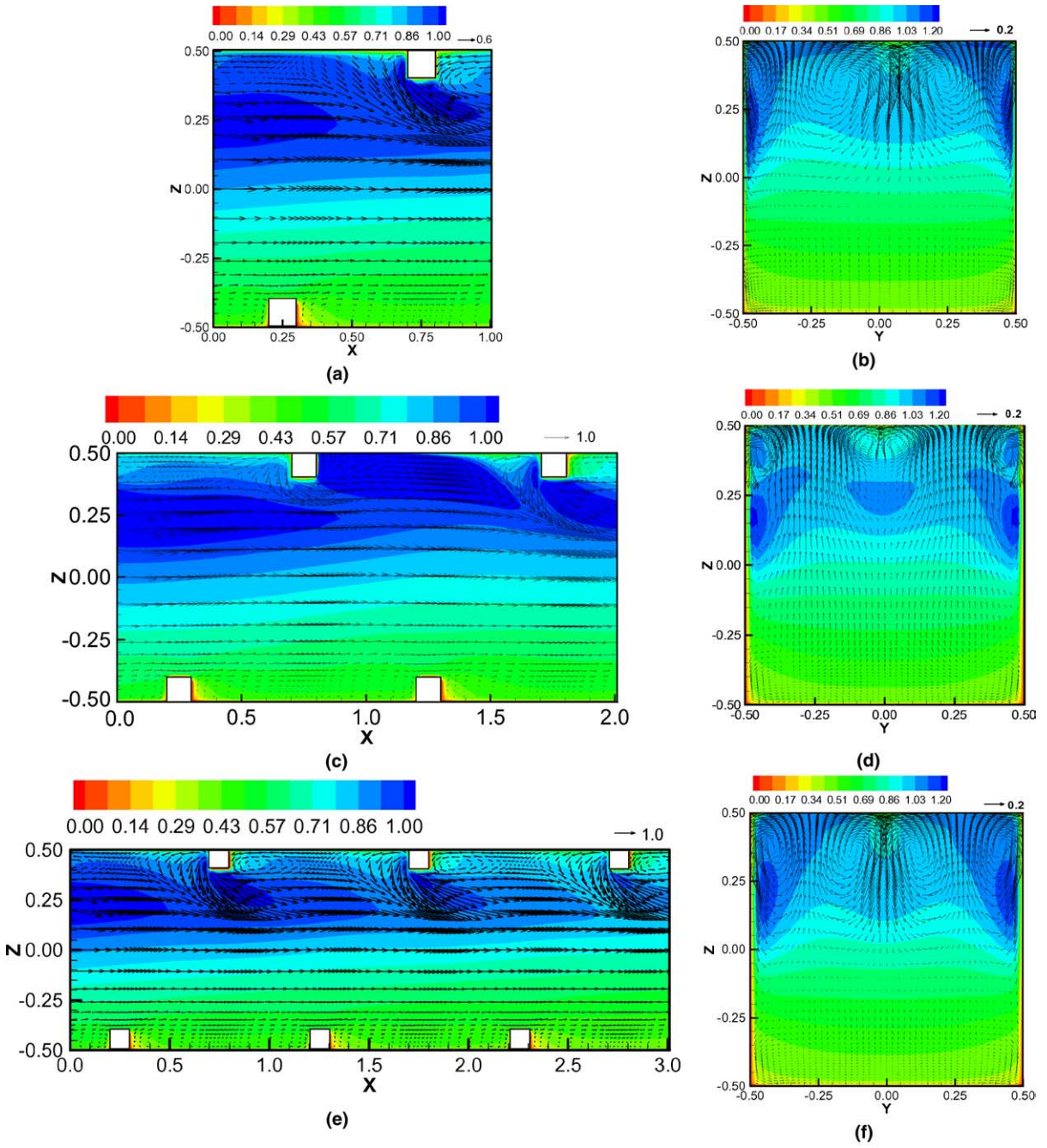

Fig. 3. Time-averaged primary (left) and secondary (right) vector field superimposed on temperature field on mid-transverse plane for $Re = 25{,}000$, DR $= 0.13$ and $Ro = 0.5$, (a, b) 1P (c, d) 2P and (e, f) 3P.

the flow structures for the 2P module reveal significantly different flow patterns, with the central pair of vortices in the 2P module being considerably smaller in size compared to the other two cases. The upwash between the central vortex and the corner vortex is stronger in the 2P module than the other two (1P and 3P) modules.

The variation of the streamwise velocity for the 1P, 2P and 3P modules at $(y,z) \equiv 0, 0.25$ is shown in Fig. 4(a). From the comparison, the significant differences between the 2P and the 1P or 3P modules is quite distinct. The 3P and the 1P module profiles are close and exhibit geometric periodicity, while the periodicity in the

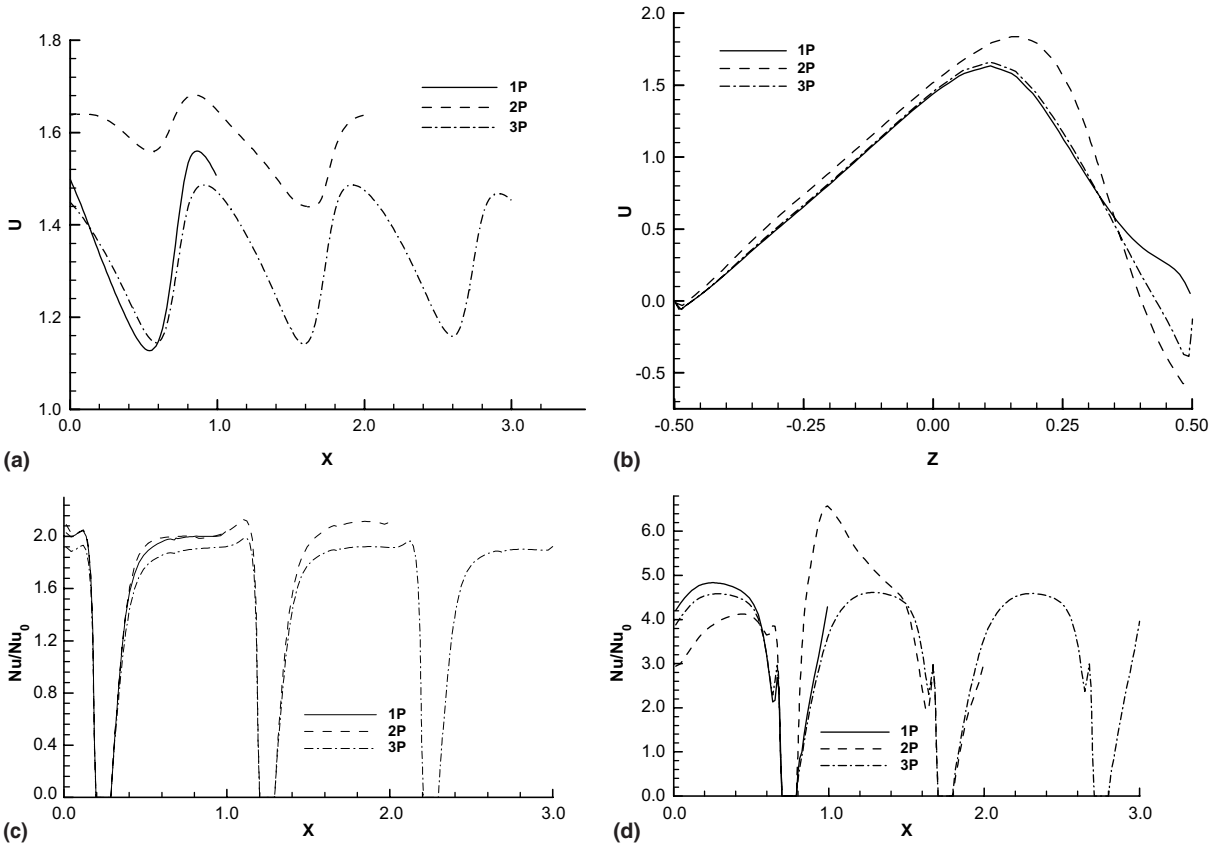

Fig. 4. 1P, 2P and 3P results of: (a) streamwise velocity vs. x at $(y,z) \equiv 0, 0.25$, (b) streamwise velocity vs. z at $(x,y) \equiv 0.5, 0$, (c) Nusselt number vs. x along the leading wall and (d) Nusselt number vs. x along the trailing wall.

2P module predictions is totally lost due to the large scale disturbances. The value of streamwise velocity is also over-predicted in the 2P module. Similarly, the transverse variation of streamwise velocity shown in Fig. 4(b) reveals the differences near the trailing wall ($z > 0$). As seen in the streamwise velocity variation, the peak value is also higher for the 2P module. It should be noted that the variation and magnitude of velocity just near the trailing wall is different even between the 1P and the 3P pitch modules, and reflects the importance of the large scale unsteadiness that is suppressed in the 1P calculations.

The streamwise variation of the spanwise averaged surface Nusselt number on the leading and trailing walls is presented in Fig. 4(c) and (d). On the leading surface, no significant difference between the 1P and 2P modules is seen. Rather, the 3P module predictions show slightly lower Nusselt numbers, but maintain their periodicity over the three periodic modules. On the other hand, the trailing wall Nusselt number (Fig. 4(d)) shows remarkably different distribution among the three modules. In the first module, the Nu value with the 1P module is higher than the 2P and the 3P module results. The loss of periodicity in the 2P module calculations is quite clear from the high peak in the Nu distribution in the second inter-rib periodic domain. However, the 3P module results exhibit periodicity in each inter-rib periodic domain.

Table 1 lists the time-averaged Nusselt number along the various confining walls of the duct for different modules for $Ro = 0.5$. The friction factor for the various cases is also given in Table 1. From the listed values of the Nusselt number, it is clear that the average heat transfer value does not vary significantly among the three different modules. The maximum difference between the 1P, 2P and the 3P modules are 1.8%, 7.3% and 7.0%, respectively, for the side-wall, leading and trailing walls, respectively. The friction factor shows a larger deviation with a maximum difference of 16% for the various cases. A similar effect of the number of periodic modules on the heat transfer is also shown in a LES study of a rotating ribbed duct by Murata and Mochizuki [18]. In their study, they investigated 1P and 3P periodic modules with inclined rounded ribs arranged in an inline fashion. Their study presents only the averaged quantities, and show good match between the 1P

Table 1
Comparison of Nusselt number and friction factor for the different periodic module

$Re = 25{,}000$, $(\Delta\rho/\rho) = 0.13$, $Ro = 0.12$	Nusselt number, Nu			Friction factor, f (per unit length)
	Side wall	Leading wall	Trailing wall	
One inter-rib periodic module	1.60	2.05	4.48	1.026
Two inter-rib periodic module	1.65	2.20	4.57	0.946
Three inter-rib periodic module	1.63	2.05	4.27	1.128

and the 3P cases, as in the present study. No flow data with different modules, except for the friction factor, has been reported in their study.

Similar to the 1:1 AR duct, the 4:1 AR duct at $Ro = 0.5$ also shows loss of periodicity across inter-rib modules. These details are not presented here, but underscore the importance of using several inter-rib modules in the calculation domain. The present calculations show that at the lower rotation numbers ($Ro = 0$, 0.12, and 0.25) a two inter-rib domain preserves periodicity across each inter-rib module, but at a $Ro = 0.5$ three inter-rib modules are necessary for the 1:1 and 4:1 AR to ensure periodicity in each inter-rib module (Figs. 3 and 4). Therefore, for all cases presented, except the 1:1 and 4:1 AR ducts at $Ro = 0.5$ that use a 3P module, results are obtained using a 2P module. While presenting results for 1:1 and 4:1 AR at $Ro = 0.5$, only the first two modules are shown although calculations are done for three inter-rib modules.

4.2. Aspect ratio of 1:1

4.2.1. Instantaneous flow

To illustrate the unsteadiness in the flow field, the temporal variation of turbulent kinetic energy ($\langle k \rangle$) is shown in Fig. 5(a) at two locations close to the leading and trailing ribbed walls ($x = 0.55$, $y = 0$, $z = \pm 0.45$) at $Ro = 0.25$. The sinusoidal nature of fluctuation shows the time-periodic behavior of the flow field, and the ability of URANS to capture large-scale unsteady behavior. The magnitude and rms of the fluctuations of k are greater near the trailing/destabilized wall compared to the leading/stabilized wall. Further the trailing wall shows additional higher frequencies not seen or prominent along the leading wall. These observations provide evidence that the Coriolis-induced secondary flows that are directed toward the trailing wall are partly responsible for destabilizing the flow field near the trailing surface. Similarly, the Nusselt number at the leading and trailing wall (plotted on different scales) shows fluctuations that have different frequencies associated with them (Fig. 5(b)). The leading wall reveals only the large-scale fluctuations (non-dimensional frequency $fD_h/u_{av} \approx 0.05$), which corresponds to the bulk fluctuation. On the other hand the, heat transfer variation on the trailing wall shows an additional high frequency oscillations and can be related to the shedding frequency (frequency ≈ 0.33) of the separated shear layer from the leading edge of the ribs on the trailing wall. Similar to the turbulent kinetic energy, the rms fluctuation of Nu is higher near the trailing wall than the leading wall.

The secondary flow generated by the Coriolis forces and the contours of streamwise velocity at various time instances (at $x = 1.0$) are presented in Fig. 6(a)–(c) for

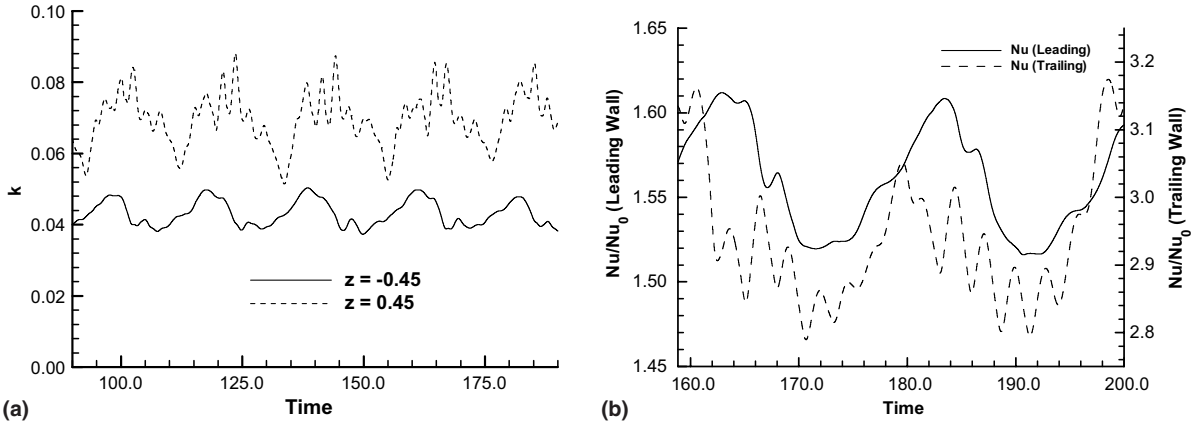

Fig. 5. (a) Temporal variation of turbulent kinetic energy at locations, at $(x, y) = (0.55, 0)$ and (b) Nusselt number variation on the leading and trailing walls at $Re = 25{,}000$, $Ro = 0.25$ and DR = 0.13. AR = 1:1.

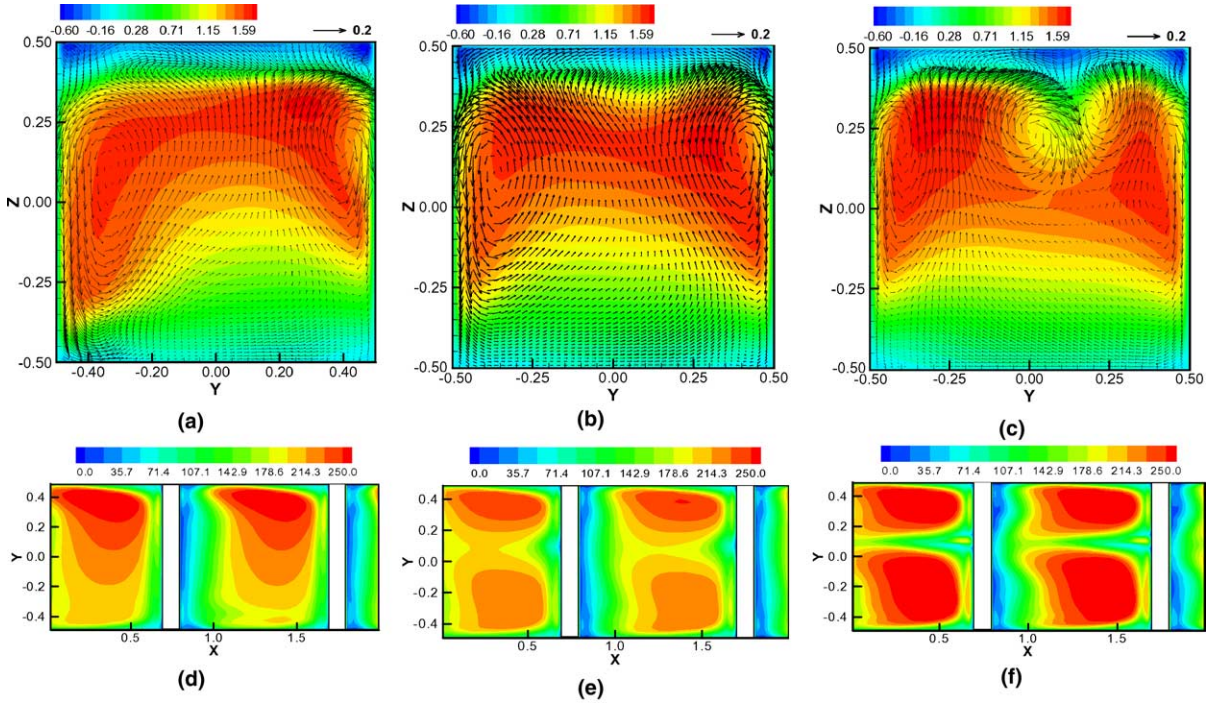

Fig. 6. Instantaneous secondary flow and streamwise velocity contours (1st row) (Top: trailing wall; Bottom: leading wall) and Nusselt number contours on the trailing wall (2nd row) ($Re = 25{,}000$, DR = 0.13 and $Ro = 0.25$) at $x = 1.0$ for: (a, d) $t = 104.14$, (b, e) $t = 109.80$ and (c, f) $t = 115.27$. AR = 1:1.

$Ro = 0.25$. The secondary flow transports cold fluid from the core of the passage towards the trailing wall and the flow descends along the two sidewalls. At the same time the hot fluid near the leading wall is also carried to the core regions by the upwash created in the secondary flow. The distinct time dependence of the secondary flow structures is quite obvious. The two unequal size counter-rotating rolls observed at $t = 104.14$ (Fig. 6(a)) are seen to change their strength and the asymmetry (Fig. 6(b)) at $t = 109.80$, and at $t = 115.27$ a second pair of rolls are seen to form near the mid-trailing wall region. At this time instance, the secondary flow is found to descend from the middle as well as along the sidewalls of the duct leading to more complex flow structures and near-wall stirring of the flow close to the trailing wall. This causes higher heat transfer on the trailing wall (Fig. 6(f)) compared to the earlier time instances (Fig. 6(d) and (e)). Note that the time scale associated with these bulk secondary flow fluctuations represent the low frequency oscillations (~0.05) in Fig. 5.

The distribution of Nusselt number on the trailing wall at the three time instances are shown in Fig. 6(d)–(f). At $t = 104.14$, there is one large patch of asymmetric high heat transfer zone between two consecutive ribs. The asymmetry is linked to a corresponding asymmetry in the streamwise velocity contours (Fig. 6(a)), which reveal that the velocity distribution near the trailing wall has a higher magnitude towards the right. On the other hand, at other two time instances, the streamwise velocity reveals a dip in its distribution near the middle of the trailing wall caused by the counter-rotating vortices (Fig. 6(b) and (c)) and its effect is clearly seen in heat transfer distribution (Fig. 6(e) and (f)).

4.2.2. Time-averaged flow

The time-averaged secondary flow superimposed on the temperature contours at $Ro = 0.12$, 0.25 and 0.50 are shown in Fig. 7(a)–(c) at $x = 0.5$. The secondary flow shows significant differences with increasing rotation number. At the lowest rotation number ($Ro = 0.12$, Fig. 7(a)), there are two large symmetric counter-rotating vortices driven by the Coriolis forces. Near the leading wall there is an additional pair of corner-vortices generated by the interaction of the separation downstream of the leading-edge rib and the Coriolis-driven secondary flows. In the separated flow region, since the streamwise velocity is directed radially-inwards, the near-wall Coriolis forces are directed toward the leading surface resulting in the corner eddies that rotate counter to the primary secondary flow vortices. The leading edge corner vortices shrink in the lateral direction while it elongates in the vertical direction as rotation number

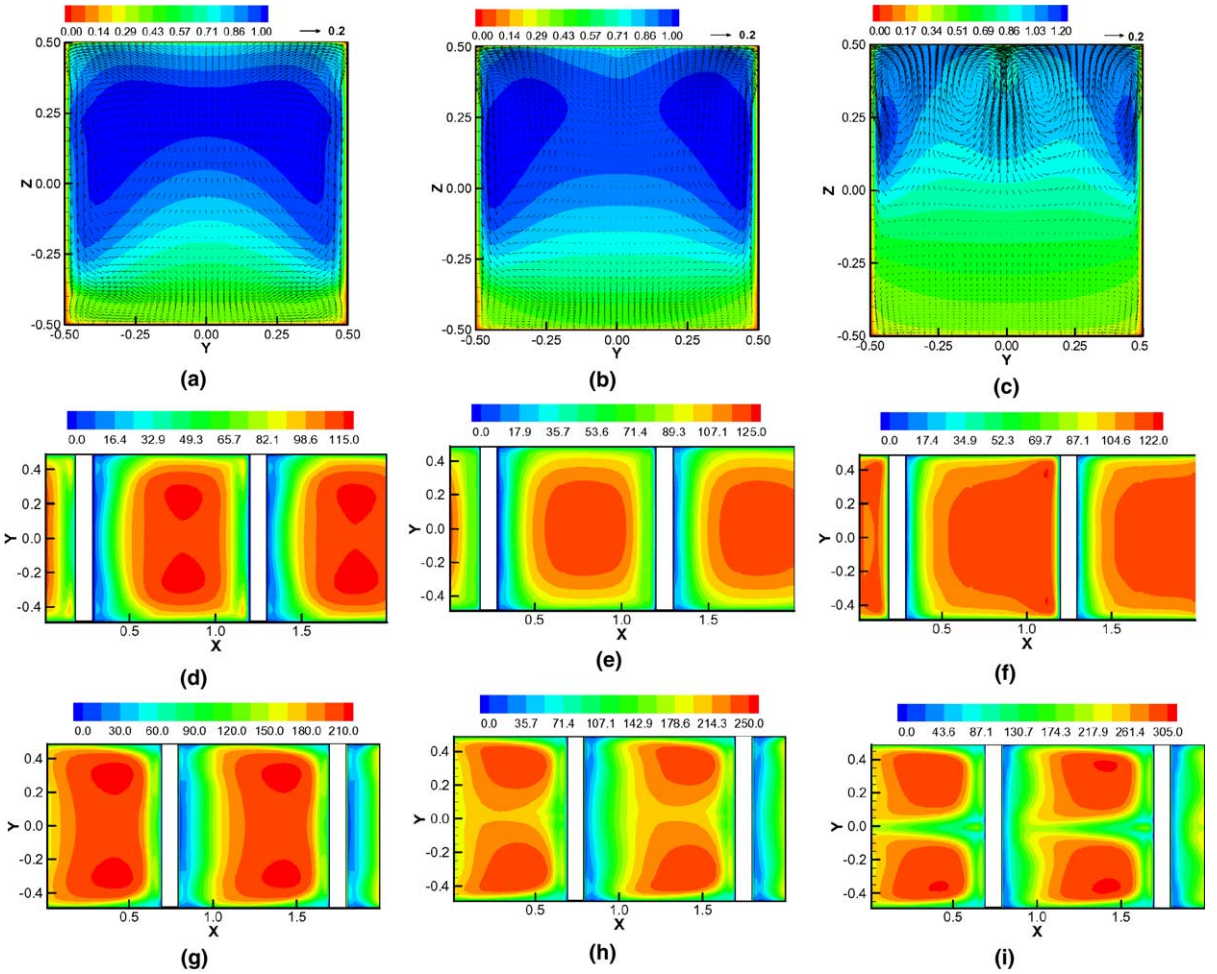

Fig. 7. Time-averaged secondary vectors and temperature contours (1st row) (a–c) at $x = 0.5$ (Top: trailing wall; Bottom: leading wall) and Nusselt number on (2nd row) leading wall (d–f) and (3rd row) trailing wall (g–i) for (a), (d) and (g) $Ro = 0.12$ (b), (e, i) $Ro = 0.25$ and (c), (f) and (i) $Ro = 0.50$. AR = 1:1.

increases to 0.25 (Fig. 7(b)). At the same time, the large counter-rotating secondary flow structures become stronger with Ro and move further towards the corners of the top trailing wall and the sidewalls, and a pair of additional vortices are formed near the middle of the trailing wall region at $Ro = 0.25$ and 0.5 (Fig. 7(b) and (c)). The temperature contours at $Ro = 0.12$ and 0.25 look similar except the colder fluid at $Ro = 0.25$ penetrates to a greater extent towards the trailing wall than at $Ro = 0.12$. The temperature distribution at $Ro = 0.5$ shows that the trailing wall region is mostly dominated by the cold fluid. The lower half of the duct ($z < 0.0$) is nearly isothermal and primarily contains heated fluid.

The variation of time-averaged Nusselt number on the two ribbed walls is shown in Fig. 7(d)–(i) at $Ro = 0.12$, 0.25, and 0.5. As expected, the trailing wall shows higher overall heat transfer than the leading wall. For all rotation numbers, the high heat transfer regions are seen to be mid-way between the ribs (where the flow typically reattaches), while the region just downstream of each rib shows a region of lower heat transfer because of the flow separation. At $Ro = 0.25$ and 0.5, the effect of secondary flow becomes more obvious on the trailing wall in the form of two peaks in the Nusselt number distribution. This is because with increasing rotation the primary secondary flow structures move toward the side walls (Fig. 7(b) and (c)), shifting the peak heat transfer coefficients outwards.

Fig. 8(a) presents the vertical variation of turbulent kinetic energy at various rotation numbers. At $Ro = 0.0$, the two high kinetic energy zones near the two walls are due to the fluctuations associated with vortex shedding from the ribs. As the rotation number is increased the fluctuation near the leading wall drops while it increases near the trailing wall. However, at $Ro = 0.5$, significantly higher fluctuations in the bulk flow are

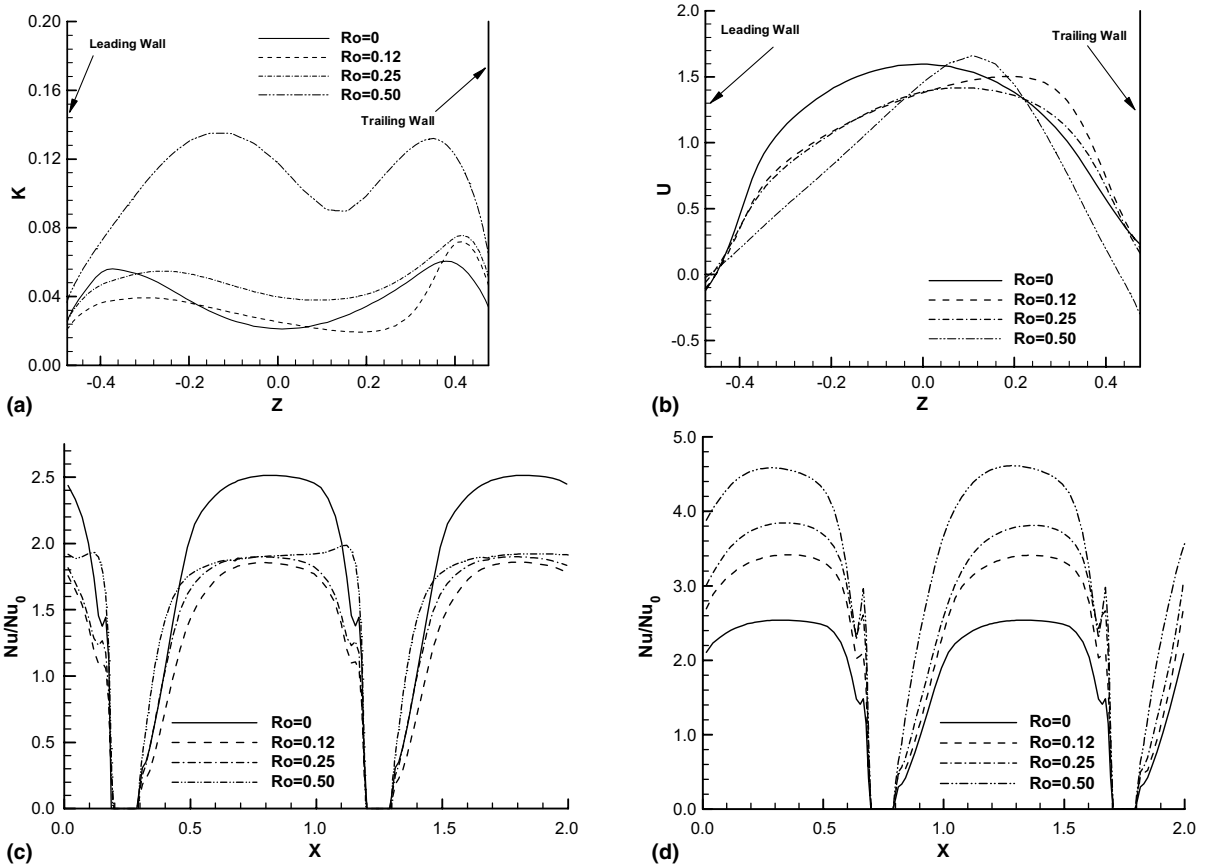

Fig. 8. Time-averaged profiles at different rotation numbers: (a) turbulent kinetic energy vs. z, (b) streamwise velocity at $(x, y) = (0.5, 0)$ vs. z, (c) spanwise averaged Nusselt number on leading wall vs. x and (d) spanwise averaged Nusselt number on trailing wall vs. x ($Re = 25{,}000$ and DR = 0.13). AR = 1:1.

observed and produces kinetic energy of comparable magnitudes near the trailing and leading walls. The vertical variation of streamwise velocity is shown in Fig. 8(b). The streamwise velocity becomes more skewed with the increase in rotation number because of the bulk flow being pushed towards the trailing due to Coriolis forces. Higher velocity gradients near the trailing wall with Ro lead to increased turbulence production, and also contribute to higher turbulence kinetic energies near the trailing wall (Fig. 8(a)).

The streamwise variation of the spanwise-averaged Nusselt number ratio (Nu/Nu_0, Nu_0 being 58.06 at $Re = 25{,}000$) is shown in Fig. 8(c) and (d). The Nu/Nu_0 on the rib surface itself is not shown for clarity. The peak heat transfer occurs near shear-layer reattachment midway between the two consecutive ribs. The trailing wall Nusselt numbers also show high Nu/Nu_0 values ahead of each rib because of the presence of the small corner eddies. As expected, with rotation the trailing wall Nu/Nu_0 increase while the corresponding leading wall values decrease; however, the leading wall values reach a minimum at Ro between 0.12 and 0.25, and increase beyond this value of Ro.

4.3. Aspect ratio of 1:4

4.3.1. Instantaneous flow

The temporal variation of turbulent kinetic energy and averaged Nusselt number ratio (normalized with the smooth channel value) on both leading and trailing walls at $Ro = 0.50$ is shown in Fig. 9. Similar to the 1:1 AR duct, the turbulent kinetic energy near the trailing wall is dominated mostly by two frequencies; the higher frequency is associated with the shedding of vortices and the large scale low frequency is associated with the bulk flow oscillation. However, no significant fluctuations are seen near the leading wall in distinct contrast with the 1:1 AR case. The heat transfer variations are shown over a smaller time scale and show that along the trailing wall the primary Nusselt number variations correspond to the higher frequency fluctuations associated with the vortex shedding. The time period of this

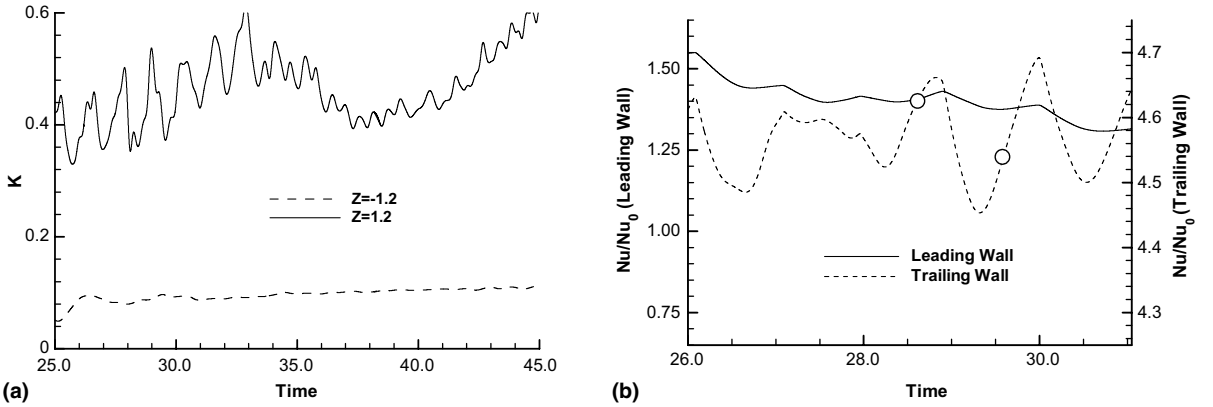

Fig. 9. Temporal variation of: (a) turbulent kinetic energy at locations, at $(x, y) = (0.55, 0)$ and (b) Nusselt number variation on the leading and trailing walls at $Ro = 0.5$ ($Re = 25{,}000$ and DR = 0.13). AR = 1:4.

heat transfer variation is however smaller (nearly half) compared to that of the square duct. This may be due to the smaller rib size compared to the vertical distance of the duct (e/D_h is same for all AR) and a lower blockage ratio of 8% compared to 20% for AR of 1. In fact, if the rib height instead of the hydraulic diameter is used to define the non-dimensional frequency, approximately the same value of the non-dimensional frequency is obtained for both aspect ratios. As expected the overall heat transfer on the trailing wall is considerably more than on the leading wall (factor of 3 or more). Note that the kinetic energy levels near the trailing wall for the 1:4 AR (Fig. 9(a)) is considerably greater (factor of 4–5) than the corresponding values for the 1:1 AR case (Fig. 5(a)), and therefore the trailing wall heat transfer enhancements are also greater for the 1:4 AR.

The instantaneous secondary velocity fields and streamwise velocity contours at two time instances over the higher-frequency time period, and at $x = 1.0$, are depicted in Fig. 10(a) and (b) for a rotation number of 0.5. The circles in Fig. 9 show the instances at which the vectors and contours are plotted. Unlike the 1:1 square duct, the leading wall region in 1:4 AR duct is dominated by multiple vortices. However, the two counter-rotating vortices in the upper-half ($z > 0$) are similar to those in a square duct but are elongated along the height due to the AR of the duct. Close to the trailing edge, corner vortices are formed, and rotate counter to the large secondary vortices. These corner vortices are a consequence of the separated flow between the ribs, and the Coriolis forces resulting from the reversed flow that produces forces directed away from the trailing surface. These structures are unsteady, and as seen in Fig. 10(a) and (b), the center of the primary vortices initially move downward, allowing the additional secondary eddy (adjacent to the primary eddy) near the trailing surface to grow (Fig. 10(a)), and then shift upwards squeezing the corners vortices (Fig. 10(b)) and decreasing their strength. The leading wall region for the 1:4 AR is populated with multiple vortices resulting from two streams of downwash hitting the leading wall. The flow in the vicinity of the leading surface becomes fully reversed at $Ro = 0.5$, and thus the Coriolis forces are directed towards the leading surface leading to the observed downwash directed to this surface. The downwash generates four counter-rotating eddies that are inherently unsteady in nature.

Fig. 10(c) and (d) show the instantaneous Nusselt number at two different time instances on the trailing walls. These distributions can be correlated with the instantaneous secondary flow patterns observed in Fig. 10(a) and (b). In the early stages of a typical dynamical pattern ($t = 28.61$), the heat transfer distribution show peak values near the corners with the heat transfer coefficients close to their peak values (Fig. 10(c)) due to the secondary flow corner vortices being stronger (Fig. 10(a)) at this time instance. At a later time, the corner eddies weaken, the core moves toward the trailing surface leading to a more spatially-uniform distribution in the heat transfer (Fig. 10(d)). These periodic variations in the trailing wall heat transfer occur over time periods that are of the order of 1.5 in non-dimensional units as depicted in Fig. 9(b).

4.3.2. Time-averaged flow

The time-averaged stream traces and the temperature distribution at mid-transverse plane has been presented for three different rotation numbers. The flow reversal of the bulk flow at higher rotation numbers ($Ro \geqslant 0.25$) is a striking feature of the 1:4 AR duct flow. Even at $Ro = 0.12$ (Fig. 11(a)), the usual flow separation and subsequent flow attachment on the leading wall is not observed. Rather, a large recirculation spanning the region between ribs and a vertical extent nearly twice the height of the ribs is obtained. With the increase in rotation number to 0.25 (Fig. 11(b)), the bulk flow

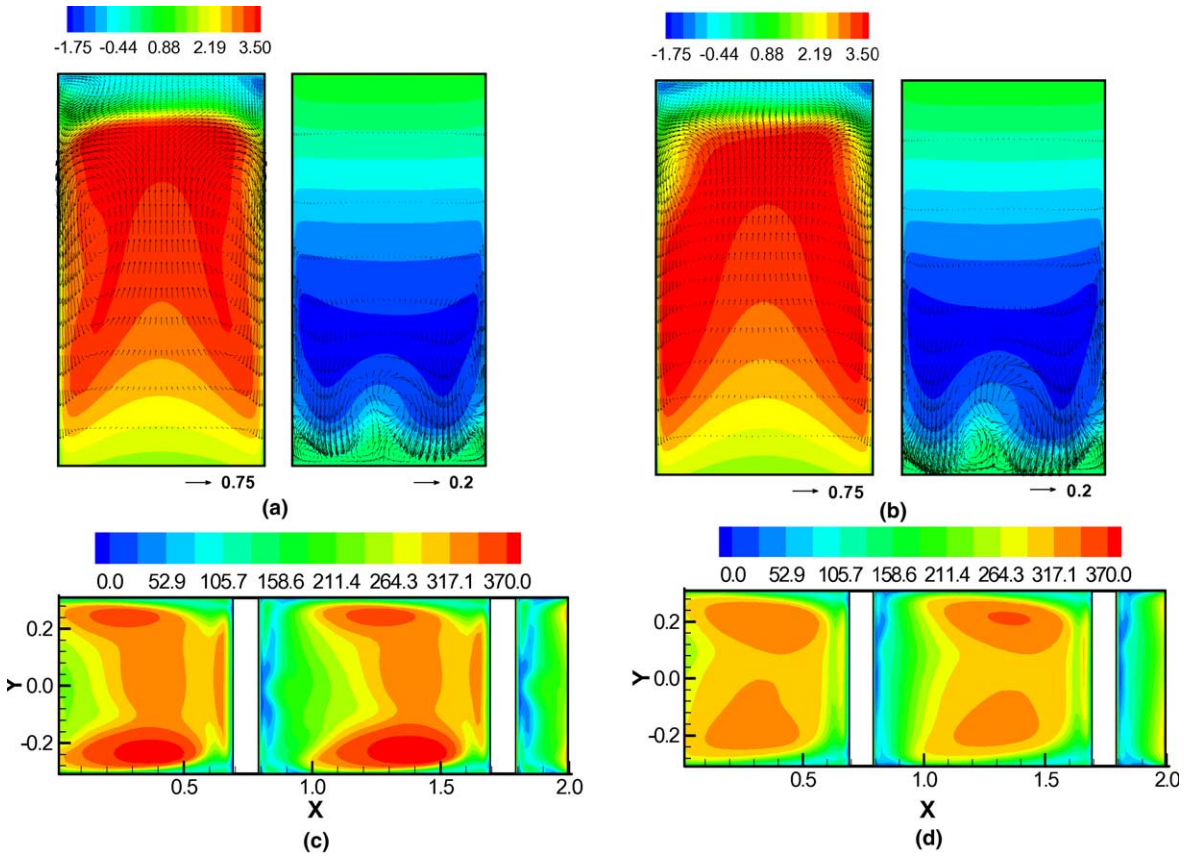

Fig. 10. Instantaneous secondary velocity vectors superimposed on streamwise velocity contours ($x = 1.0$) (1st row) (a–b) and Nusselt number contours on trailing wall (2nd row) (c–d) for $Ro = 0.50$ ($Re = 25{,}000$ and DR = 0.13) at (a, c) $t = 28.61$ and (b, d) $t = 29.58$. AR = 1:4.

reverses near the leading wall region of the duct. Both the Coriolis forces that push the flow away from the leading surface and the centrifugal-buoyancy, which retards the flow, are responsible for the flow reversal near the surface. Because of the flow moving outward from the leading surface, the reversed streamlines and velocity vectors do not exhibit a rib-induced separation or eddy. When the rotation number is further increased ($Ro = 0.50$), a larger extent of the bulk flow is reversed and enhances the Coriolis force that is directed towards the leading wall. Since the average flow rate is maintained constant the trailing wall velocities are correspondingly increased. At $Ro = 0.50$ (Fig. 11(c)), the reversed flow is so strong that the leading edge flow separates past the rib and generates separated eddies similar to that on the trailing wall but on opposite sides of the ribs. Dutta et al. [26] have reported full reversal of the flow for a 1:1 AR smooth channel, and have concluded that buoyancy is responsible for the reversed flow.

Since the flow reverses along the leading wall at a specific Ro (for a specified Re and DR), there is a critical point(s) in the parameter space (Re, Ro and DR) where the flow along the leading surface will be stagnant. To identify these critical points, calculations would be needed for a finer parameter space matrix, and has not been performed in the present study. However, for stagnant-flow conditions, the leading surface Nusselt numbers will be very low (conduction-limited), and surface temperature is likely to spike leading to potential blade failures.

The time-averaged secondary flow and the superimposed temperature contours are depicted in Fig. 11(d)–(f) at $x = 0.5$. At this location, the flow is mostly attached on the trailing surface. Therefore, the Coriolis forces and the secondary flows are directed toward the trailing wall, and a two-roll vortex is observed without the additional small corner vortex pair observed near the trailing surface (as in Fig. 10 at $x = 1.0$). Near the leading surface, the flow field at high Ro is fully reversed, resulting in a Coriolis force directed toward the surface generating a four-roll flow pattern for $Ro = 0.25$ and a two-roll flow pattern for $Ro = 0.50$. Closer examination of the secondary flow structures at the three rotation numbers reveals that the vertical extent of the large

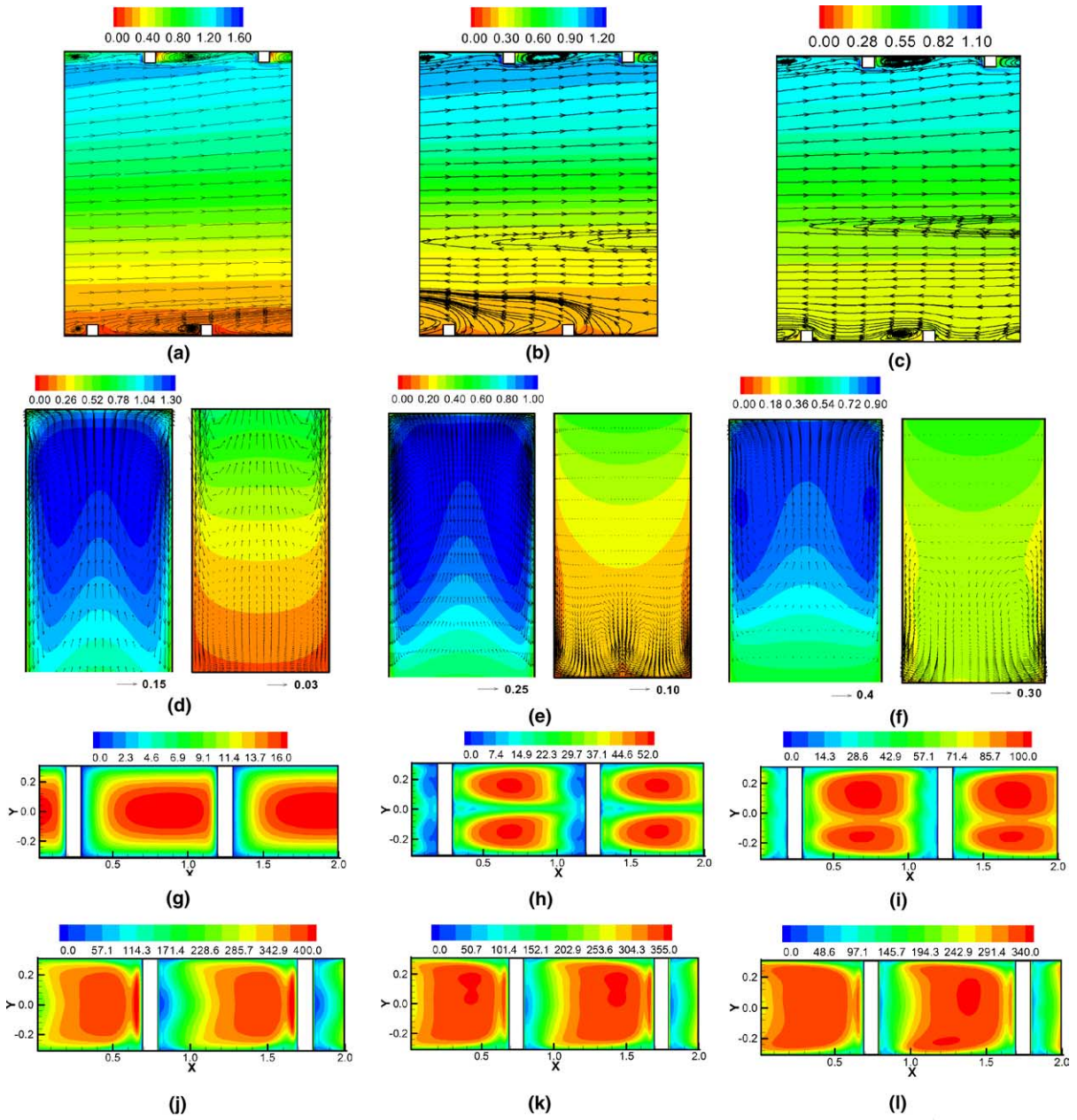

Fig. 11. Time-averaged primary flow field and temperature contours at $y = 0$ (a–c) (1st row), time-averaged secondary flow field and temperature contours (d–f) (2nd row) (Top: trailing wall; Bottom: leading wall) and contours of time-averaged Nusselt number on leading wall (g–i) (3rd row) and trailing wall (j–l) (4th row) for (a), (d), (g) and (j) $Ro = 0.12$ (b), (e), (h) and (k) $Ro = 0.25$ and (c), (f), (i) and (l) $Ro = 0.50$ ($Re = 25{,}000$ and DR = 0.13). AR = 1:4.

counter rotating vortex pair decreases with the increase in rotation number. The decrease in size is associated with an increase in the strength of the vortices. Regarding the temperature distribution, the bottom part of the duct is dominated by high temperature fluid at the low rotation number. With the increase in rotation number, the magnitude of the reversed bulk flow velocity increases and results in a decrease in temperature of the bulk flow near the leading wall region.

The surface heat transfer on both the leading and trailing walls is shown in Fig. 11(g)–(l) for the three rotation numbers. At the low rotation number ($Ro = 0.12$)

one large patch of high heat transfer is observed along the leading surface, while at $Ro = 0.25$ and 0.50, two regions of high Nusselt numbers are observed. At low rotation number secondary vortices near the leading wall are not strong, and the heat transfer is primarily influenced by the separation and reattachment of the bulk primary flow. On the other hand, the two patches of high heat transfer on the leading surface at $Ro = 0.25$ are caused by the two strong downwash streams seen in the secondary flow patterns in Fig. 11(d)–(f). The strong secondary flow at high rotation number makes the bulk primary flow strongly three-dimensional near the leading wall. It is observed that the maximum value of Nusselt number increases significantly (by a factor of 3) when the rotation number is increased from 0.12 to 0.25, and by a factor of nearly 5 when Ro is increased further to 0.50. The axial flow velocity near the leading wall at $Ro = 0.12$ is lower than the reversed flow velocity at $Ro = 0.25$, and the backflow magnitude increases further when the rotation number is increased from $Ro = 0.25$ to 0.50 (see Fig. 11(a)–(c)). This increase in the reversed flow velocity increases the heat transfer on the leading wall. Since the flow is fully reversed, the upstream corner eddy, usually associated with a Nu-peak, is not observed here.

The heat transfer distribution on the trailing surface does not show significant variation with different rotation numbers. Rather, as seen in Fig. 12(d), there is a fourfold increase in Nu/Nu_0 when Ro is increased from 0 (stationary) to 0.12, beyond which no substantial increase in Nu/Nu_0 occurs with increasing Ro. The key difference in the three contours in Fig. 11(j)–(l), is that, the low heat transfer region downstream of each rib shrinks in size as the rotation number is increased.

Fig. 12(a) shows the profiles of turbulent kinetic energy as a function of vertical distance, z at the location $x = 0.5$. As expected, the turbulent kinetic energy is the highest near the unstable trailing wall where strong

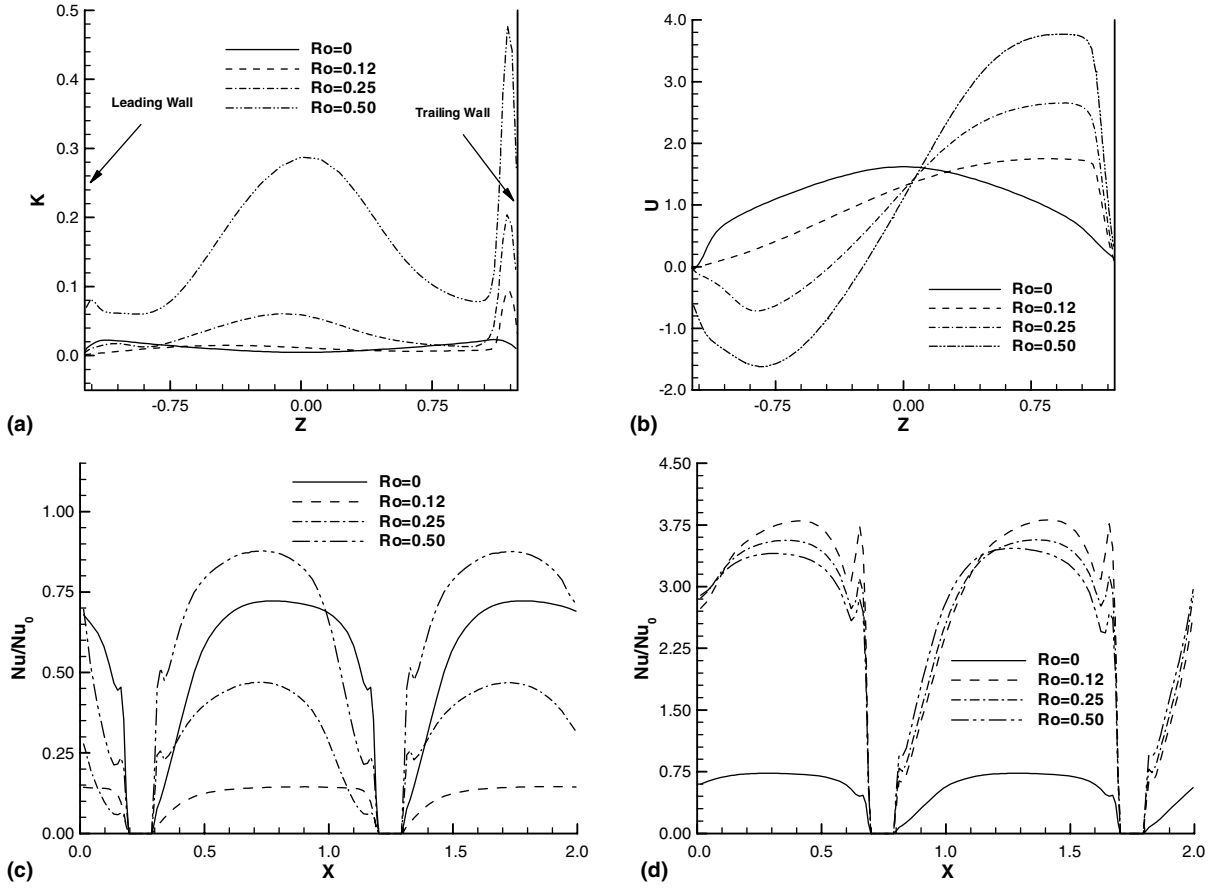

Fig. 12. Time-averaged profiles at different rotation numbers: (a) turbulent kinetic energy vs. z, (b) streamwise velocity at $(x, y) = (0.5, 0)$ vs. z, (c) spanwise averaged Nusselt number on leading wall vs. x and (d) spanwise averaged Nusselt number on trailing wall vs. x ($Re = 25{,}000$ and DR = 0.13). AR = 1:4.

shear layers are present, and increases with Ro. However, there is an additional peak in the middle for the two high rotation numbers namely, $Ro = 0.25$ and 0.50. The reason for this bulge in the kinetic energy profile is the flow reversal in the bulk flow seen in Fig. 11(b) and (c), where due to counter-shear, turbulence production is high. The variation of streamwise velocity at various rotation numbers is also presented in Fig. 12(b) at $x = 0.5$. The bulk velocity profile at $Ro = 0$ shows behavior similar to the plane Poiseuille flow as the blockage is small (8%). On the other hand, the bulk velocity distribution at $Ro = 0.12$ shows a continuous increase from the leading towards the trailing wall. At high rotation numbers ($Ro = 0.25$ and 0.50) bulk flow reversal is seen near the leading wall. The maximum values of the reversed flow is -0.72 and -1.60 at $Ro = 0.25$ and 0.50, respectively.

The spanwise-averaged surface heat transfer on both leading and trailing wall is illustrated in Fig. 12(c) and (d). At $Ro = 0.12$, the peak heat transfer on the leading wall is significantly lower compared to the square duct heat transfer (factor of 10), and is lower (by a factor of nearly 4) than the stationary value. As noted earlier, for certain combinations of Re, Ro, and DR, the flow is expected to stagnate leading to very low, conduction-limited Nusselt numbers. However, beyond a Ro of 0.12, the leading wall reveals a significant increase in Nu/Nu_0 with the increase in rotation number from 0.12 to 0.5. This is attributed to the strengthening of the reversed flow along the leading surface, but even at a relatively high Ro of 0.25, the Nu/Nu_0 values are below the stationary condition. On the trailing surface, as noted earlier, at $Ro = 0.12$ there is greater than a four-fold increase in heat transfer over the stationary value, while no such strong dependence is seen beyond $Ro = 0.12$. Unlike the square duct, the temperature and flow periodicity over a unit geometrically-periodic module is maintained for the 1:4 AR duct.

4.4. Aspect ratio of 4:1

4.4.1. Instantaneous flow

The temporal variation of turbulent kinetic energy at a location $(x, y) \equiv 0.55, 0$ and the Nusselt number on the leading and trailing walls are depicted in Fig. 13 for $Ro = 0.25$. The low frequency fluctuation of the turbulent kinetic energy near the trailing wall (solid line) is much higher than that along the leading wall, but the kinetic energy magnitude is comparable or lower (over the time range presented in Fig. 13) to that near the leading wall. This is in contrast to the observations for the 1:1 AR and 1:4 AR ducts where kinetic energy levels near the trailing wall were higher than those along the leading wall. The reason for comparable magnitudes is due the close proximity of the two ribbed walls, and the multi-roll secondary flow patterns (shown later). For the same reason, the Nusselt numbers on both walls do not deviate significantly from each other (Fig. 13(b)) as that of the other two AR ducts.

The instantaneous secondary velocity vectors superimposed on the temperature field at two time instances are presented in Fig. 14(a) and (b) for a rotation number of 0.25. The interesting feature of the flow field is that multiple pairs of counter-rotating rolls (generally four) are present in the 4:1 AR duct. The enlarged view of the two sidewalls regions is also shown. For the 4:1 AR duct it appears that the core fluid from the center is directed both toward the trailing surface and the leading surface, with the centers of the resulting counter-rotating vortices located close to the trailing surface. The vortices near the two sidewalls transport flow down to the leading surface leading to high heat transfer in the corner regions. The vortices in the middle also transport flow to the leading wall. Thus, unlike other AR, the leading wall for the 4:1 AR always sees secondary flow directed towards it. Such a flow pattern is likely to enhance the leading wall heat transfer relative to other

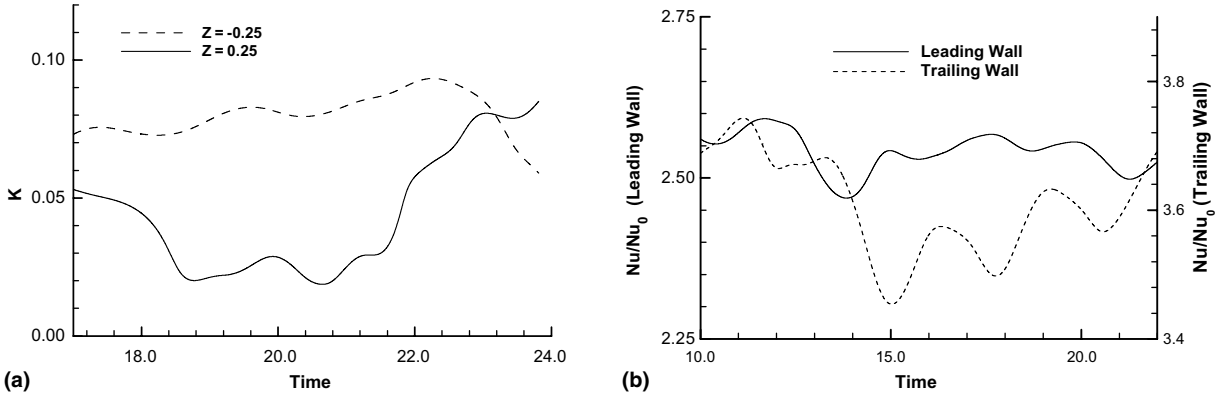

Fig. 13. Temporal variation of: (a) turbulent kinetic energy at locations, at $(x, y) = (0.55, 0)$ and (b) Nusselt number variation on the leading and trailing walls at $Ro = 0.25$ ($Re = 25{,}000$ and DR = 0.13). AR = 4:1.

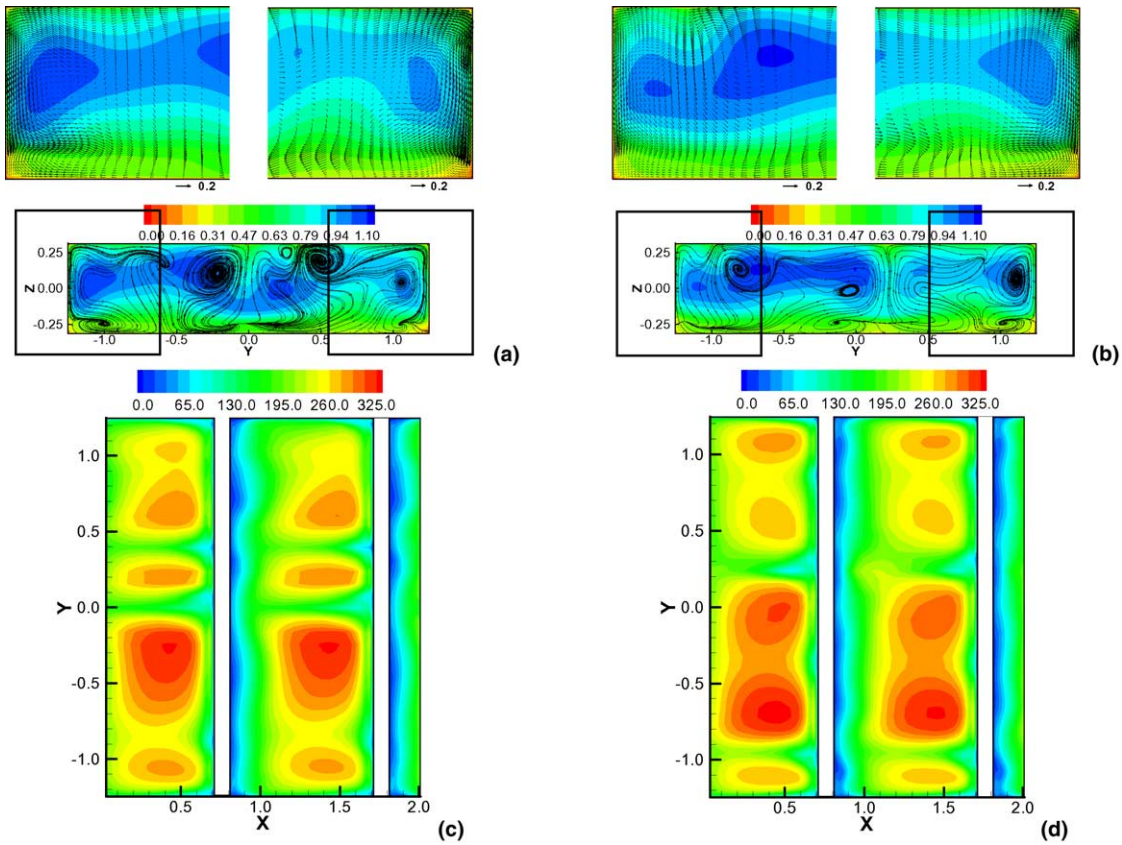

Fig. 14. Instantaneous secondary velocity vectors superimposed on temperature contours at $x = 0.5$ (a–b) (1st row) (Top: trailing wall; Bottom: leading wall) and Nusselt number distribution on trailing wall (c–d) (2nd row) ($Ro = 0.25$ and DR = 0.13) (a, c) $t = 29.32$ and (b, d) $t = 36.75$. AR = 4:1, ($Re = 25{,}000$ and DR = 0.13).

AR cases, and this observation is borne out from the Nusselt number plots (Figs. 13(b), 15 and 16). Furthermore, the disparity between trailing and leading surface heat transfer rates are likely to be the lowest for this AR since both surfaces see secondary flows directed toward them, although the proximity of the eye of the recirculating vortices to the trailing surface still ensures higher heat transfer on this surface. The temperature contours also show considerable variation in their distribution with time. As for the other AR ducts, the colder fluid near the trailing wall is indicative of the effect of Coriolis force that pushes the bulk flow towards the trailing wall. Since the bulk flow is populated with multiple vortices, the variation of temperature appears to be somewhat correlated to the secondary motion, especially in the region with stronger secondary flow.

Fig. 14(c) and (d) show the instantaneous Nusselt number distribution on the trailing wall at $Ro = 0.25$. The multiple patches of high heat transfer region are clearly visible corresponding to the multiple rolls seen in Fig. 14(a) and (b). A strong time-dependence in the surface heat transfer is distinctly observed from Fig. 14(c) and (d). Clearly the dynamics of the secondary flows are strong enough to influence the surface Nusselt numbers significantly.

4.4.2. Time-averaged flow

Fig. 15(a) and (b) present the time-averaged secondary flow structures along with the temperature contours for the two rotation numbers ($Ro = 0.12$ and 0.25). Even in the time-averaged flow field, the existence of multiple rolls is quite clear. Comparison of the two plots at the two Ro does not reveal any significant topological variation although the positions and orientation of the rolls do not match between the two rotation numbers, and there is a lack of symmetry around the $y = 0$ plane. This may be caused due to low frequency (long time period) unsteadiness associated with the flow, and the inadequate averaging time (same averaging time as for the AR 1:1 and 1:4 was used). The strength of the secondary flow for the 4:1 AR at all rotation numbers is found to be the least among the three AR ducts.

The time-averaged heat transfer distribution on the two ribbed walls are presented in Fig. 15(c)–(f). The heat

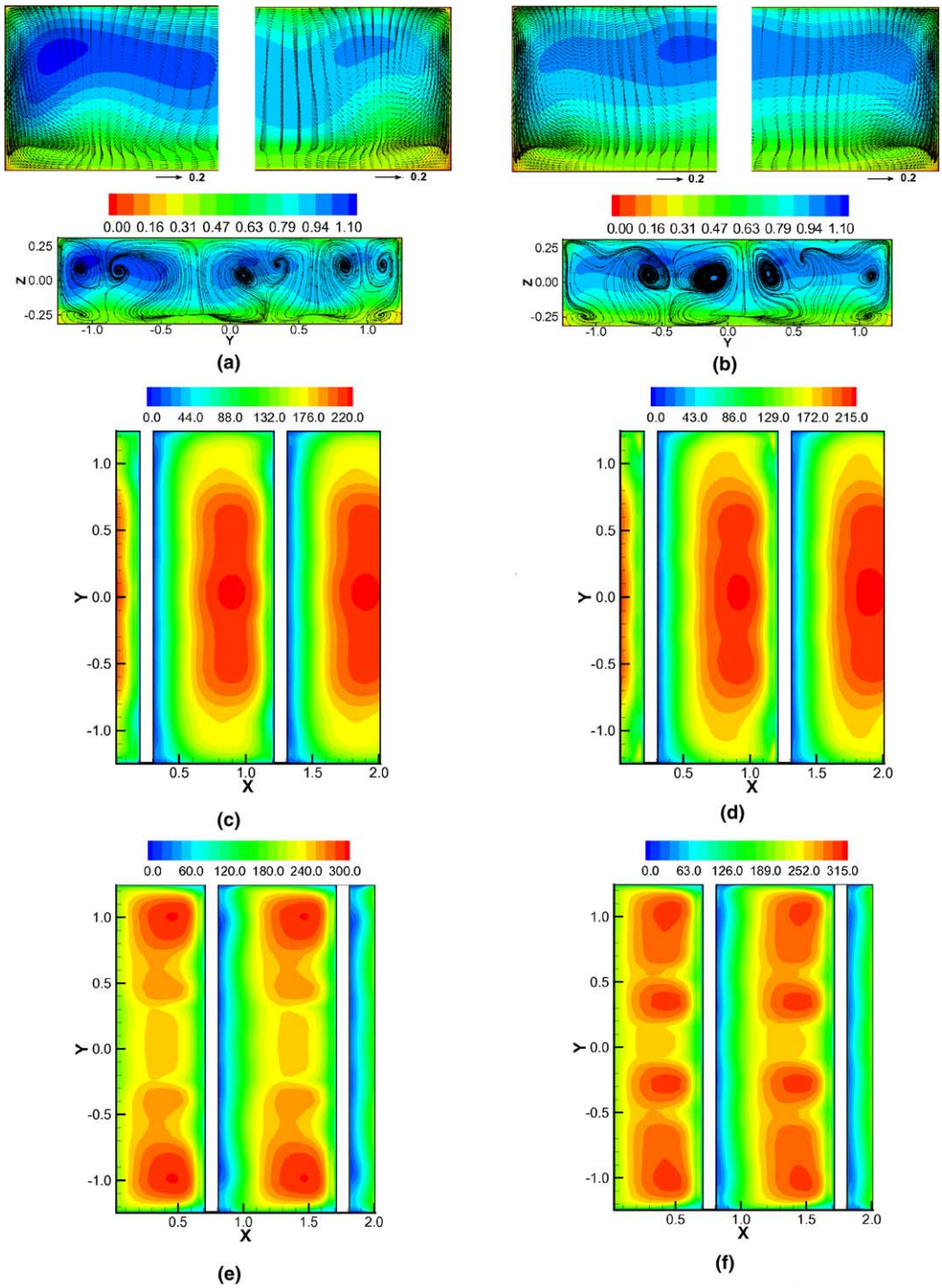

Fig. 15. Time-averaged secondary vectors and temperature contours (1st row) (a–b) at $x = 0.5$ (Top: trailing wall; Bottom: leading wall) and Nusselt number on (2nd row) leading wall (c–d) and (3rd row) trailing wall (e–f) for (a), (c) and (e) $Ro = 0.12$ (b), (d) and (f) $Ro = 0.25$ ($Re = 25{,}000$ and DR = 0.13). AR = 4:1.

transfer distribution on the leading wall for the two low rotation numbers ($Ro = 0.12$ and 0.25) is almost similar while the trailing wall shows an increase in the number of high heat transfer patches with Ro. As noted earlier,

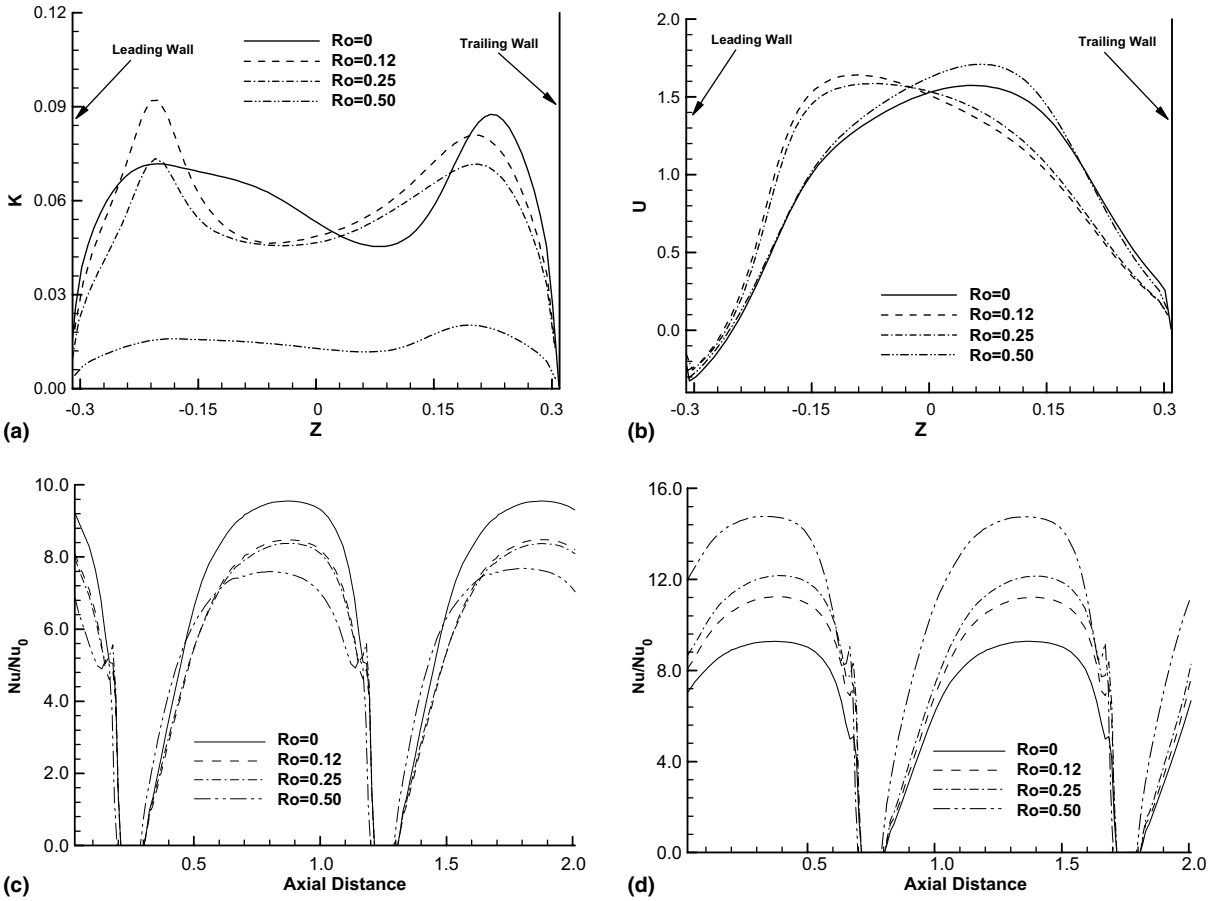

Fig. 16. Time-averaged profiles at different rotation numbers: (a) turbulent kinetic energy vs. z, (b) streamwise velocity at $(x, y) = (0.5, 0)$ vs. z, (c) spanwise averaged Nusselt number on leading wall vs. x and (d) spanwise averaged Nusselt number on trailing wall vs. x ($Re = 25{,}000$ and DR = 0.13). AR = 4:1.

the differences in the peak Nu between the leading and trailing surfaces are not as large as in the other AR cases, and the reasons for this were attributed to the downward directed secondary flows along the leading surface.

The vertical variation of turbulent kinetic energy at $(x, y \equiv 0.5, 0)$ has been plotted in Fig. 16(a). Twin peaks in the profile are observed at the lower rotation numbers ($Ro = 0.12$ and 0.25). These twin peaks are partly due to the higher velocity gradient in the secondary flow near both walls caused by the presence of ribs. The turbulent kinetic energy is found to decrease with the increase in rotation number. It is interesting to note that the turbulent kinetic energy drops significantly once rotation number increases from 0.25 to 0.50. This is because of the fact that at $Ro = 0.50$, the multi-roll secondary flow structures are altered and the whole cross flow region is mostly dominated by two large secondary recirculatory bubbles. The streamwise velocity variation in the vertical direction is shown in Fig. 16(b). At $Ro = 0.50$, the streamwise velocity is skewed to the trailing wall as it expected. On the contrary, the velocity at two low rotation numbers are skewed towards the leading wall, which is somewhat surprising. This is because of the secondary flow directed toward the leading surface as noted earlier. However, no significant variation in the maximum velocity magnitude has been observed.

The spanwise averaged axial Nusselt number variation on both the walls is depicted in Fig. 16(c) and (d). The variation looks similar to the other AR ducts except the Nusselt number values are higher, and the differences between the leading and trailing surfaces are lower. On the leading wall, at all rotation numbers, similar variation having equal magnitude of Nusselt number is discerned. The insensitivity to the rotation number is again linked to the secondary flows directed to the leading surface (rather than away from it as observed at 1:1 and 1:4 AR cases). On the other hand, the trailing wall reveals an increase in heat transfer with rotation number due to the intensification of the counter-rotating vortices.

4.5. Comparison of various AR

Table 2 presents the averaged (time and space averaged) Nusselt number for various aspect ratios and rotation numbers. In general, the heat transfer at the leading wall shows a decrease while it increases at the trailing wall with rotation. The square duct shows a systematic increase in Nusselt number with Ro at all confining walls for $Ro > 0.12$. Johnson et al. [5] report that in the lower rotation number range (0–0.23), there is a decrease in Nusselt number ratio on the leading wall, but beyond $Ro = 0.23$ the Nusselt number ratio increases with further increase in rotation. The same behavior is seen here except the minimum point is located for a Ro between 0.12 and 0.25. At high rotation numbers (>0.25), Coriolis and buoyancy effects become significant causing an increase in the leading wall heat transfer. The heat transfer on the sidewalls increases with rotation due to the secondary flow caused by Coriolis force acting normal to the flow direction. The relative increase in heat transfer is maximum for the trailing wall (93%) while the sidewalls and leading wall show increases of 45% and −7%, respectively, when rotation is increased from 0 to 0.50.

The leading wall of 1:4 AR duct shows surprisingly low heat transfer at low rotation number (below 1 for rotation number of $\leqslant 0.25$). As discussed earlier, the leading wall region is dominated by a large separation at $Ro = 0.12$ and the core experiences backflow at $Ro \geqslant 0.25$. Therefore, the velocity is reduced near the leading wall leading to a corresponding decrease in heat transfer. With increasing rotation number the strength of the backflow increases, resulting in an increase in the Nusselt number values. The magnitude of the heat transfer on the trailing and side walls is higher than the square duct values at all rotation numbers. The relative increase in Nu/Nu_0 between $Ro = 0$ and 0.5 are 42%, 14% and 368% for the sidewalls, the leading and the trailing wall, respectively. The trailing wall shows significantly higher Nu/Nu_0 than the leading wall relative to the square duct.

The heat transfer for 4:1 AR duct reveals no significant difference in the leading and trailing wall heat transfer contrary to that observed in 1:4 and 1:1 AR duct. However, similar to the 1:1 AR, Nusselt number on all walls increases with an increase in rotation number beyond $Ro = 0.12$. As Ro is increased from 0 to 0.50, the relative increase in heat transfer for the side, leading and trailing walls are 57%, −10% and 24%, respectively. Comparison of all AR duct shows that the difference in heat transfer between the leading and trailing walls decreases with the increase in aspect ratio. The heat transfer on the sidewalls also increases with the increase in AR.

The friction loss in a ribbed duct depends on the size of the ribs that contribute to the form drag and the strength of the secondary flows. For $Ro = 0.12$, where the core flow does not experience flow reversal, the friction factor is minimum for 1:4 AR duct while it is the most for 4:1 AR duct. The blockage in the duct, which is least (8%) for the 1:4 AR duct and highest (32%) for 4:1 AR duct, is one of the primary reasons for the high friction factor for the 4:1 AR duct. For 1:1 AR duct, the sudden increase in friction factor at $Ro = 0.50$ is due to the strong secondary flow associated at this rotation number. Similarly, the 1:4 AR duct shows a sudden increase in friction factor at $Ro = 0.25$ because of the flow reversal that takes place in the bulk flow and this trend increases with rotation number. At $Ro = 0.50$, the 4:1 AR duct also shows a sudden jump in the friction factor value. The probable reason for such an increase is the transition that takes place in the secondary flow structures in which multiple rolls are found to collapse to form a pair of large vortices.

Table 2
Nusselt number and friction factor for the various cases

Aspect ratio	Rotation number	Nusselt number, Nu			Friction factor, f (per unit length)
		Side wall	Leading wall	Trailing wall	
1:1	0.00	1.14	2.37	2.37	0.1484
	0.12	1.46	1.71	3.16	0.1949
	0.25	1.54	1.84	3.54	0.3528
	0.50	1.63	2.05	4.27	1.128
1:4	0.00	1.88	1.11	1.11	0.0521
	0.12	2.68	0.18	6.05	0.1459
	0.25	2.46	0.63	5.37	0.4983
	0.50	2.66	1.26	5.20	1.7843
4:1	0.00	2.03	3.34	3.33	0.4786
	0.12	3.30	2.96	3.98	0.5576
	0.25	3.24	2.98	4.03	0.7503
	0.50	3.19	3.01	4.12	1.5300

5. Conclusions

The flow and heat transfer in a ribbed duct with aspect ratios of 1:1, 4:1 and 1:4 are investigated numerically using an unsteady RANS procedure. The following are some key observations.

- For all AR coolant passages, the flow field is found to exhibit large-scale unsteadiness. At least two inter-rib modules have to be included in the streamwise periodic direction to predict flow unsteadiness. However, at $Ro = 0.5$ the calculation domain has to be extended to three inter-rib modules for the 1:1 and 4:1 AR in order to maintain periodic behavior in each inter-rib module.
- For AR 1:1, the flow unsteadiness appears to be characterized by two time-scales, with one corresponding to the Coriolis-driven secondary flow unsteadiness (longer time scale) and the other corresponding to the vortex roll up associated with the separated shear layer (shorter time-scale). The unsteadiness (particularly that associated with the separated shear layer) is greater along the trailing surface, and is also seen in the Nusselt number distributions. Similar observations are made for the 4:1 AR where the bulk secondary flow unsteadiness is primarily important, and for the 1:4 AR where the unsteadiness and turbulence kinetic energy along the trailing surface is quite strong, and the unsteadiness along the leading surface is relatively weak.
- The 1:4 AR duct shows flow reversal at high rotation number with multiple rolls in the secondary flow structures near the leading wall. The bulk separation along the leading surface produces a Coriolis-driven downwash and multi-roll secondary flows near the leading surface.
- The relative difference between the trailing wall and leading wall heat transfer is the highest in 1:4 AR duct. For certain parameter values, the leading wall flow is expected to become stagnant leading to conduction-limited heat transfer.
- The 4:1 AR duct shows the evidence of multiple rolls in the secondary flow that direct the core flow to both the leading and trailing surfaces. Therefore the difference between the leading and trailing wall heat transfer in the 4:1 AR duct is not significant like in the other two aspect ratio cases. The average Nusselt number (all walls) is the highest for the 4:1 case.
- The increase in rotation number beyond $Ro = 0.25$ increases the heat transfer on all confining walls except the trailing wall in 1:4 AR duct which is relatively insensitive to increases in rotation number beyond 0.12. Reduction in the leading wall heat transfer occurs only up to a Ro in the range of 0.12–0.25. A significant increase in friction factor occurs at the highest Ro studied ($Ro = 0.5$) due to the strengthening of the secondary flows and changes in the flow pattern.

Acknowledgements

This work was supported by a grant from South Carolina Institute of Energy Studies (SCIES) under the DOE-University Turbine Systems Research (UTSR) program. Support was also received from the Louisiana Board of Regents through the Clean Power and Energy Research Consortium (CPERC) and from the LSU Center for Computation and Technology.

References

[1] J.C. Han, J.S. Park, Developing heat transfer in rectangular channel with rib turbulators, Int. J. Heat Mass Transfer 31 (1) (1988) 183–195.
[2] J.C. Han, Heat transfer and friction characteristics in rectangular channels with rib turbulators, J. Heat Transfer 110 (1988) 321–328.
[3] J.H. Wagner, B.V. Johnson, R.A. Graziani, F.C. Yeh, Heat transfer in rotating serpentine passages with trips normal to the flow, J. Turbomach. 114 (1992) 847–857.
[4] B.V. Johnson, J.H. Wagner, G.D. Steuber, F.C. Yeh, Heat transfer in rotating serpentine passages with trips skewed to the flow, J. Turbomach. 116 (1994) 113–123.
[5] B.V. Johnson, J.H. Wagner, G.D. Steuber, Effect of rotation on coolant passage heat transfer, NASA Contractor Report-4396, vol. II, 1993.
[6] Y. Chen, D.E. Nikitopoulos, R. Hibbs, S. Acharya, T.A. Myrum, Detailed mass transfer distribution in a ribbed coolant passage, Int. J. Heat Mass Transfer 43 (2000) 1479–1492.
[7] F. Zhou, J. Lagrone, S. Acharya, Internal cooling in 4:1 AR passages at high rotation numbers, ASME Paper GT2004-53501, 2004.
[8] T.S. Griffith, L. Al-Hadhrami, J.C. Han, Heat transfer in rotating rectangular cooling channels (AR = 4) with angled ribs, J. Heat Transfer 124 (2002) 617–625.
[9] P. Agarwal, S. Acharya, D.E. Nikitopoulos, Heat transfer in 1:4 rectangular passages with rotation, J. Turbomach. 125 (2003) 726–733.
[10] D.L. Rigby, E. Steinthorsson, A.A. Ameri, Numerical prediction of heat transfer in a channel with ribs and bleed, ASME Paper 97-GT-431, 1997.
[11] T. Bo, H. Iacovides, B.E. Launder, Developing buoyancy-modified turbulent flow in ducts rotating in orthogonal mode, J. Turbomach. 117 (1995) 474–484.
[12] H. Iacovides, Computation of flow and heat transfer through rotating ribbed passage, Int. J. Heat Fluid Flow 19 (1988) 393–400.
[13] M. Al-Qahtani, Y.-J. Jang, H.C. Chen, J.C. Han, Prediction of flow and heat transfer in rotating two-pass rectangular channels with 45° rib turbulators, J. Turbomach. 124 (2) (2002) 242–250.

[14] M. Al-Qahtani, H.C. Chen, J.C. Han, A numerical study of flow and heat transfer in rotating rectangular channels (AR = 4) with 45° rib turbulators by Reynolds stress turbulence model, J. Heat Transfer 125 (1) (2003) 19–26.

[15] J. Pallares, L. Davidson, Large eddy simulations of turbulent flow in a rotating square duct, Phys. Fluids 12 (11) (2000) 2878–2894.

[16] A.K. Saha, S. Acharya, Flow and heat transfer in internally ribbed ducts with rotation: an assessment of LES and RANS, J. Turbomach. 127 (2) (2005) 306–320.

[17] A. Murata, S. Mochizuki, Large eddy simulation with a dynamic subgrid-scale model of turbulent heat transfer in an orthogonally rotating rectangular duct with transverse rib turbulators, Int. J. Heat Mass Transfer 43 (7) (2000) 1243–1259.

[18] A. Murata, S. Mochizuki, Effect of cross-sectional aspect ratio on turbulent heat transfer in an orthogonally rotating rectangular duct with angled rib turbulators, Int. J. Heat Mass Transfer 46 (16) (2003) 3119–3133.

[19] G. Wang, S.P. Vanka, Convective heat transfer in periodic wavy passages, Int. J. Heat Mass Transfer 38 (17) (1995) 3219–3230.

[20] M. Kato, B.E. Launder, The modelling of turbulent flow around stationery and vibrating square cylinders, in: Proc. 9th Symp. on Turbulent Shear Flows, Kyoto, Japan, vol. 10-4, 1993.

[21] F.H. Harlow, J.E. Welch, Numerical calculation of time-dependent viscous incompressible flow of fluid with free surfaces, Phys. Fluids 8 (1965) 2182–2188.

[22] T. Kawamura, H. Takami, K. Kuwahara, Computation of high Reynolds number flow around a circular cylinder with surface roughness, Fluid Dyn. Res. 1 (1986) 145–162.

[23] A.K. Saha, S. Acharya, Large eddy simulation of flow and heat transfer in a periodic rib-roughened rotating square duct, in: Proc. 9th Symposium on Transport Phenomena and Dynamics of Rotating Machinery, Honolulu, Hawai, USA, 2002.

[24] A.K. Saha, S. Acharya, Parametric study of unsteady flow and heat transfer in a pin–fin heat exchanger, Int. J. Heat Mass Transfer 46 (20) (2003) 3815–3830.

[25] A.K. Saha, G. Biswas, K. Muralidhar, Two-dimensional study of the turbulent wake behind a square cylinder subject to uniform shear, J. Fluids Eng. 123 (2001) 595–603.

[26] S. Dutta, M.J. Andrews, J.C. Han, Prediction of turbulent heat transfer in rotating smooth square ducts, Int. J. Heat Mass Transfer 39 (12) (1996) 2505–2514.